Research Square

Preprints are preliminary reports that have not undergone peer review.
They should not be considered conclusive, used to inform clinical practice,
or referenced by the media as validated information.

Normal Brain Irradiation Promotes Breast Cancer Brain Metastasis via Senescent Astrocyte-Mediated Blood-Brain Barrier Disruption and HGF/c-Met/PI3K/AKT Activation

Shiyu Cheng
Zhongnan Hospital of Wuhan University
Yuan Ke
Zhongnan Hospital of Wuhan University
Linhui Zheng
Zhongnan Hospital of Wuhan University
Jingtian Yu
Zhongnan Hospital of Wuhan University
Gong Zhang
Zhongnan Hospital of Wuhan University
Zhiyuan Xiong
Zhongnan Hospital of Wuhan University
Yue Liu
Zhongnan Hospital of Wuhan University
Wanyu Chen
Zhongnan Hospital of Wuhan University
Dong Liu
Zhongnan Hospital of Wuhan University
Chaoyan Wu
Zhongnan Hospital of Wuhan University
Haijun Yu
haijunyu@whu.edu.cn
Zhongnan Hospital of Wuhan University

Research Article

Keywords: breast cancer brain metastasis, brain irradiation, astrocyte senescence, HGF/c-Met/PI3K/AKT signaling pathway, blood–brain barrier

Posted Date: November 19th, 2026

DOI: https://doi.org/10.21203/rs.3.rs-11606767/v1

License: This work is licensed under a Creative Commons Attribution 4.0 International License.
Read Full License

Additional Declarations: No competing interests reported.

Abstract

Background

Whether irradiation of normal brain tissue creates a pro-metastatic microenvironment for breast cancer brain metastasis (BCBM) remains unclear. We investigated astrocyte senescence as a potential upstream link between brain irradiation and BCBM.

Methods

Mice received 10 Gy brain irradiation 30 days before internal carotid artery injection of 4T1-Luc cells. Metastatic colonization, blood-brain barrier (BBB) integrity, astrocyte senescence, and HGF/c-Met/PI3K/AKT signaling were assessed. ABT-263 was administered before tumor injection to clear senescent astrocytes.

Results

Prior irradiation enhanced early brain colonization and metastatic progression, increased BBB permeability, and shortened survival. Irradiation induced astrocyte senescence and a senescence-associated secretory phenotype. Senescent astrocytes impaired BBB integrity and secreted hepatocyte growth factor, activating c-Met/PI3K/AKT signaling in breast cancer cells. ABT-263 cleared senescent astrocytes, reduced BBB leakage and brain metastasis, and prolonged survival.

Conclusions

Normal brain irradiation can establish a pro-metastatic microenvironment through astrocyte senescence, which links BBB disruption and HGF/c-Met/PI3K/AKT activation to promote BCBM. Astrocyte senescence is thus a key upstream event connecting brain irradiation with BCBM and a potential therapeutic target.

1. Introduction

According to the latest data released by the International Agency for Research on Cancer (IARC) of the World Health Organization in 2022, female breast cancer is the second most common malignancy worldwide, with approximately 2.3 million new cases (11.6%), after lung cancer (approximately 2.5 million cases, 12.4%).[1] Brain metastasis is a leading cause of death in patients with breast cancer, severely affecting both survival and quality of life. Compared with hormone receptor-positive/human epidermal growth factor receptor 2 (HER2)-negative breast cancer, triple-negative breast cancer (TNBC) and HER2-positive breast cancer are more prone to brain metastasis, with incidences exceeding 35% and 40%, respectively.[2] Once brain metastasis occurs, the disease progresses rapidly; moreover, due to the

presence of the blood–brain barrier (BBB), drug delivery to the lesion is limited, resulting in poor treatment outcomes and an unfavorable prognosis .[3] Although significant progress has been made in the treatment of breast cancer brain metastasis over the past two decades, it remains a major cause of patient mortality.[4]

The metastatic process of breast cancer from the primary site to the brain is complex and involves a four-step cascade: (i) epithelial–mesenchymal transition (EMT) and cell detachment; (ii) intravasation of cancer cells into peripheral blood vessels; (iii) initiation of the brain metastatic niche; and (iv) extravasation and brain colonization.[5] Each step involves multiple genetic mutations and intricate molecular pathways.[6]

Whole-brain radiotherapy (WBRT) is an important local treatment modality for brain metastases and has demonstrated efficacy in controlling intrabrain lesions and alleviating neurological symptoms.[7] However, accumulating clinical and preclinical evidence in recent years suggests that radiotherapy, while killing tumor cells, may also exert a “double-edged sword” effect by remodeling the tumor microenvironment.[8] Following brain irradiation, resident brain cells such as astrocytes and microglia undergo complex phenotypic changes that may, through paracrine mechanisms, affect BBB function and tumor cell behavior, thereby paradoxically promoting tumor invasion and metastasis.[9] This radiotherapy-induced facilitation of distant tumor growth, which contributes to treatment failure, has also been termed the “abscopal” effect.[10]

Astrocytes are critically involved in preserving the integrity of the blood-brain barrier (BBB) and maintaining the homeostasis of the neural microenvironment, representing the most abundant glial cell population in the central nervous system (CNS).[11] Recent studies have shown that ionizing radiation induces a senescent phenotype in astrocytes, accompanied by activation of the senescence-associated secretory phenotype (SASP).[12] SASP factors include a variety of pro-inflammatory cytokines, chemokines, and growth factors, which can remodel the microenvironment and promote malignant progression of tumor cells.[13] Nevertheless, whether radiotherapy-induced astrocyte senescence contributes to the promotion of breast cancer brain metastasis, and the mechanistic links between astrocyte senescence, BBB disruption, and activation of tumor signaling pathways, remain poorly understood.

The present study aimed to investigate the role and molecular mechanisms of astrocyte senescence induced by brain irradiation in breast cancer brain metastasis. We hypothesized that brain irradiation promotes brain metastasis by inducing astrocyte senescence through two synergistic mechanisms: on one hand, senescence of astrocytes, which serve as structural support cells, compromises BBB integrity; on the other hand, SASP factors secreted by senescent astrocytes activate the c-Met/PI3K/AKT signaling pathway in breast cancer cells, collectively facilitating metastatic colonization and progression. To test this hypothesis, we established a mouse model of breast cancer brain metastasis via internal carotid artery injection and performed transcriptomic sequencing, in vitro co-culture systems, and in vivo rescue experiments using the senolytic agent ABT-263. Through multi-level in vivo and in vitro

approaches, the present study systematically elucidated a molecular pathological cascade in which irradiation induces astrocyte senescence, leading to BBB disruption and tumor signaling activation, thereby promoting brain metastasis progression. This study aims to provide new theoretical foundations and therapeutic targets for optimizing radiotherapy strategies in breast cancer brain metastasis.

2. Methods

Cell Culture and Reagents

The mouse triple-negative breast cancer cell line 4T1, along with GFP-4T1 and 4T1-Luc stable transfectants generated by lentiviral transduction (Procell), were used in this study. All cell culture and storage procedures were performed strictly according to the manufacturer's instructions, and detailed steps are provided in the supplementary materials.

In Vitro Co-culture of Cells

To investigate the interaction between breast cancer cells and astrocytes, indirect and direct contact co-culture systems were established using 4T1 (Procell), GFP-labeled 4T1, and the mouse astrocyte cell line C8D1A (Procell). Indirect co-culture was performed using two methods: Transwell inserts (0.4 um, NEST) and conditioned medium.

The groups were as follows: (i) control group: 4T1 cells cultured alone; (ii) experimental group 1: 4T1 cells co-cultured with non-irradiated C8D1A cells; (iii) experimental group 2: 4T1 cells co-cultured with irradiated C8D1A cells. To determine the optimal radiation dose, C8-D1A cells were exposed to graded doses (2, 4, 6, and 8 Gy) in preliminary experiments, and 4 Gy was selected for subsequent in vitro irradiation of astrocytes.

For the Transwell co-culture system, 4T1 cells (1×10^5 cells/well) were seeded into the upper chamber (0.4 um, NEST), while C8D1A cells (2×10^5 cells/well) were seeded into the lower chamber of six-well plates. For experimental group 2, C8D1A cells were irradiated one day prior to co-culture. After 24 or 48 hours of co-culture, 4T1 cells in the upper chamber were collected for subsequent phenotypic assays, including assessments of migration, invasion, proliferation, and apoptosis.

For the conditioned medium co-culture system, C8D1A cells (2×10^5 cells/well) received either non irradiated (experimental group 1) or irradiation (experimental group 2) one day prior to co-culture. The following day, supernatants were collected from each group. Conditioned medium was mixed with fresh culture medium at a 1:1 ratio, and the mixture was added to adherent 4T1 cells that had been seeded in six-well plates (2×10^5 cells/well) at 2 mL per well. After 24 or 48 hours of stimulation, 4T1 cells were collected for the same phenotypic analyses.

For direct contact co-culture, irradiated or non-irradiated C8D1A cells were co-cultured with GFP- 4T1 cells at a 1:1 ratio in large culture dishes.

Transwell Migration and Invasion Assays

To assess the migration and invasion abilities of 4T1 tumor cells following co-culture, Transwell chambers (8.0 um, Corning) and Matrigel (Beyotime, Cat. No. C0371) were used.[14] Detailed cell numbers are listed as follows: 1×10^5 cells/well in 200 μL for migration assays; 2.5×10^5 cells/well in 200 μL for invasion assays. The lower compartment was supplemented with medium containing 10% fetal bovine serum, which served to attract cells. For the in vitro rescue experiments, following treatment of the co-culture supernatant from the irradiated group with Mouse HGF-neutralizing antibody (R&D Systems, Catalog No. AF2207, 1 ug/mL), tumor cells were then processed for subsequent assays. Subsequent steps are described in the supplementary materials. All experiments were performed in triplicate and independently repeated at least three times.

Cell Proliferation Assay

We quantified the short-term and long-term proliferation of 4T1 cells using CCK-8 and colony formation assays, respectively. Procedural details can be found in the supplementary materials.

Flow Cytometric Apoptosis Assay

Apoptosis of tumor cells was detected using the Annexin V-FITC dual-staining kit (Beyotime, C1062L) combined with flow cytometry. All procedures were performed strictly according to the manufacturer's instructions. Detailed steps are provided in the supplementary materials.

Fluorescence-Activated Cell Sorting (FACS)

To isolate the two cell populations from the direct contact co-culture system for separate analyses, fluorescence-activated cell sorting (FACS) was performed. Cells to be sorted (GFP-4T1 and C8D1A cells from direct contact co-culture) were collected, washed, and resuspended in pre-chilled PBS containing 2% fetal bovine serum (FBS) to prepare a single-cell suspension at a density of approximately 1×10^7 cells/ml. The suspension was filtered through a 40 μm cell strainer into sterile FACS tubes to remove cell clumps. Based on the experimental design, target cell populations were gated using the appropriate fluorescence channel (the GFP channel for GFP-labeled 4T1 cells; unlabeled cells were identified as C8D1A cells) on a flow cytometric cell sorter. Sterile sheath fluid was used during the sorting process, and collection tubes were pre-filled with an appropriate amount of complete culture medium containing 20% FBS to preserve cell viability. Sorted cells were immediately placed on ice, and a small aliquot was taken for purity assessment to ensure that the sorting purity met the experimental requirements (typically > 90%). The sorted C8D1A cells were then used directly for subsequent RNA extraction and RT-PCR analyses.

ELISA

To quantify the levels of various secreted factors in the co-culture system, supernatants were collected from the experimental and control groups, and the concentrations of secreted factors were determined

using ELISA kits. The following ELISA kits were used: Mouse TNF-α ELISA Kit (ABclonal, Cat. No. RK00027), Mouse HGF ELISA Kit (ABclonal, Cat. No. RK00371), Mouse IFN-γ ELISA Kit (ABclonal, Cat. No. RK00019), Mouse TGF-β ELISA Kit (ABclonal, Cat. No. RK00057), and Mouse VEGF ELISA Kit (Kerui). All assays were performed according to the manufacturer's instructions.

qRT-PCR

To determine the mRNA expression levels of secretory factors in astrocytes, quantitative real-time RT-PCR (qRT-PCR) was performed. Total RNA was extracted from sorted C8D1A cells using Trizol reagent. RNA purity and concentration were assessed spectrophotometrically. The procedural details and primers used in this study are listed in the supplementary materials.

In Vitro Endothelial Permeability Assay

To evaluate endothelial permeability under different treatment conditions, FITC-dextran (40kDa, 1 mg/mL; Sigma-Aldrich, USA) was used, and changes in endothelial permeability were assessed based on the concentration of dextran that penetrated the endothelial monolayer.[15] To establish an in vitro monolayer barrier, bEnd.3 (mouse brain microvascular endothelial cell line) harvested from the various treatment groups were plated onto the apical compartment of Transwell inserts (0.4 um, NEST). After 24 hours, when the endothelial cells had adhered, 100 ul of FITC-dextran solution was added to the upper chamber, and 500 ul of blank culture medium was added to the lower chamber. Following a 1-hour incubation in the dark, the medium in the lower chamber was collected, and its fluorescence intensity was measured using a fluorescence spectrophotometer (Thermo Fisher Scientific, USA) to reflect changes in endothelial cell permeability. The experiment was independently repeated three times, and the dextran leakage rate was calculated for each group.

Single-Nuclei RNA Sequencing(snRNA-Seq)

C8D1A and bEnd.3 cells from different treatment groups were collected for Single-Nuclei RNA Sequencing (RNA-Seq), with three biological replicates per group.

Protein Extraction and Western Blotting

The procedures for protein extraction and western blotting were identical to those described previously.[16] Detailed protocols and antibody information are provided in the supplementary materials. The experiment was independently repeated three times.

Animal Studies

Female BALB/c mice (4–6 weeks old) were purchased from Biogen (Hubei, China). Mice were anesthetized with isoflurane and immobilized for brain irradiation. Brain irradiation was performed using an X-ray device (X-Rad) in the anterior–posterior position, which was equipped with a specially designed collimator to deliver an isodose exposure field with a diameter of 10 mm. The irradiation parameters

were set as follows: 6 MV X-rays, source-to-skin distance (SSD) of 100 cm, field size of 35 × 35 cm^2, and absorbed dose rate of 200 cGy/min. The experimental group received a single dose of 10 Gy per mouse. Based on the brain depth of 8-week-old mice (0.75 cm) and the dose rate, the irradiation time was calculated to be 5 minutes. The bodies of the mice outside the irradiation field were protected using a lead shield. Control animals were subjected to a mock irradiation session. Following these procedures, all mice were kept in a standard laboratory environment and were routinely checked for weight loss as well as other indicators of mucositis.

Mouse Brain Metastasis Model

A mouse model of brain metastasis was established using intracarotid artery injection technique.[17]The detailed procedures were as follows: Female BALB/c mice (6–8 weeks old) were anesthetized with isoflurane inhalation and fixed on a microsurgical platform. A 1-cm incision was made in the throat skin. The right common carotid artery was exposed, and the external carotid artery was ligated. A polyurethane catheter (0.1 mm) was then inserted into the common carotid artery to deliver cells into the internal carotid artery. Luciferase-labeled 4T1 tumor cells (4T1-Luc; 3 × 10^5 cells per mouse in 100 ul of sterile PBS) were slowly injected. The injection speed was adjusted according to the mouse's respiration and heart rate monitored during the procedure. The arteries upstream and downstream of the injection site were ligated, after which the catheter was removed, and the throat wound was closed with silk suture. Mice were kept warm until they regained consciousness. Brain colonization of tumor cells was analyzed by in vivo bioluminescence imaging at 24 and 48 hours, as well as 3, 5, 7, and 9 days after injection. Mice were regularly monitored for body weight loss and brain metastasis progression, and received anti-infection treatment and routine care.

In the therapeutic efficacy study, mice received ABT-263(MeilunBio, MB4611, 10mg/kg, p.o.) or vehicle (60% phosphate buffer, 10% ethanol, 30% PEG-400) by oral gavage on alternate days, with a total of seven administrations starting 14 days after brain irradiation. Subsequently, brain metastasis was established by intracarotid artery injection of tumor cells, and brain metastasis progression in the treatment groups was monitored by bioluminescence imaging.

Tumor-bearing mice were euthanized when they exhibited signs of distress, including lethargy, reduced activity, severe kyphosis, leg dragging, ruffled fur, or body weight loss. Brain tissues were collected for subsequent pathological analyses. Brains were fixed in 4% paraformaldehyde (PFA) for 1 hour and embedded in paraffin for paraffin sectioning, or embedded in Tissue-Tek OCT compound at 4°C for frozen sectioning. All animal studies were approved by the Institutional Animal Care and Use Committee (IACUC) of the Animal Experiment Center of Wuhan University (approval No. 210971413).

In Vivo Bioluminescence Imaging (IVIS)

To monitor the progression of brain metastasis in each group of mice, bioluminescence imaging was performed using an IVIS Lumina imaging system (Xenogen Corporation) and its accompanying data acquisition software, following the manufacturer's instructions. Prior to imaging, mice were anesthetized

with isoflurane inhalation and intraperitoneally injected with D-luciferin potassium salt solution (180 mg/kg, dissolved in PBS; Beyotime). Images were acquired at the peak luminescence time point, 10 minutes after injection. The photon flux was quantified within the luminescent region using Living Image analysis software to reflect the bioluminescence signal intensity of the tumors. Statistical analysis was performed on the data from each group.

Blood–Brain Barrier Permeability Assay

To evaluate BBB permeability in each group of mice, FITC-dextran (40kDa, Sigma-Aldrich, USA) was used, and BBB leakage was assessed based on the concentration of penetrated dextran.[18] Mice in the control and experimental groups (post-radiotherapy) were intravenously injected via the tail vein with FITC-dextran solution (40 mg/kg, dissolved in sterile PBS). After circulation for 1 hour, the mice were perfused with physiological saline through the heart to remove residual fluorescent dye from the vasculature. Brain tissues of interest were rapidly isolated and prepared for frozen sections. Fluorescence signals of perivascular leakage were observed and quantitatively analyzed on frozen sections using a fluorescence microscope. Changes in BBB permeability were assessed based on fluorescence intensity or leakage area. Three to five biological replicates were used per group.

Histopathology

At the experimental endpoint, mice were anesthetized with isoflurane inhalation and transcardially perfused with ice-cold 0.01 M PBS until the outflow was clear, followed by perfusion fixation with 4% paraformaldehyde (pH 7.4). Whole brains were completely removed and fixed in 4% paraformaldehyde for 48 hours. The paraffin sections were stored at room temperature for subsequent hematoxylin and eosin (H&E) staining, Ki67 staining, and immunofluorescence assays.

For H&E staining, brain sections were dewaxed in xylene, rehydrated through a graded ethanol series, stained with hematoxylin solution for 5–10 minutes, rinsed under running water for blueing, and then counterstained with eosin solution for 1–3 minutes. After further dehydration through graded ethanol and clearing in xylene, the sections were mounted with neutral balsam. The pathological morphology of tumor cells and the number of metastatic foci in brain tissues were observed under a light microscope and statistically analyzed. Three to six biological replicates were used per group.

Immunohistochemistry (IHC)

Protein extraction and western blotting were carried out following protocols described in previous studies.[16] Detailed procedures and antibody information are listed in the supplementary materials.

Immunofluorescence (IF)

As described above, after dewaxing, rehydration, heat-induced antigen retrieval, and blocking, the sections were incubated with corresponding primary antibodies overnight at 4°C. On the following day, after three washes with PBS, the sections were exposed to fluorescence-labeled secondary antibodies

for 1 hour at room temperature under dark conditions. After counterstaining the nuclei with DAPI, the sections were mounted with an anti-fade mounting medium. Images were observed and captured using a fluorescence microscope or confocal microscope. For each section, 5–10 high-power fields were randomly selected in the target region for quantitative analysis of fluorescence signals. Three to six biological replicates were used per group. The antibodies used are provided in the supplementary.

SA-β-Gal

To assess astrocyte senescence following radiotherapy, SA-β-Gal staining was performed using a SA-β-Gal staining kit (Beyotime, Cat. No. C0602) on cultured mouse astrocytes (C8D1A) before and after irradiation (in vitro experiments), as well as on brain sections before and after irradiation (in vivo experiments).[19] All steps were performed following the manufacturer's guidelines. After staining, we use a Leica bright-field microscope to capture images. The percentage of SA-β-Gal-positive cells was counted for each group in both cultured cells and brain sections. Three replicates were performed per group.

Statistical Analysis

All experiments were carried out with a minimum of three biological replicates, and the results are expressed as mean ± standard error of the mean (SEM). Statistical analyses were performed using GraphPad Prism software (version 10.4.2; GraphPad Software, USA). Unpaired two-tailed Student's t-test was used for direct comparisons between two groups, and analysis of variance (ANOVA) was used for multiple group comparisons. Survival curves were estimated using the Kaplan–Meier method and compared using the log-rank test. A P value < 0.05 was considered statistically significant.

3. Results

3.1 A Murine Model of Breast Cancer Brain Metastasis after Normal Brain Irradiation

Recent studies have shown that most mouse models of breast cancer brain metastasis are established by delivering tumor cells via the heart or major blood vessels.[20] To investigate the effect of brain irradiation on breast cancer brain metastasis, 4T1-Luc cells were inoculated into the mouse brain via internal carotid artery injection (Fig. 1A, D). The experimental procedure is shown in Fig. 1A. Mice received brain irradiation (10 Gy) under fluoroscopic guidance to ensure uniform whole-brain exposure (Fig. 1B). Thirty days after irradiation, 4T1-Luc cells were delivered by internal carotid artery injection, and brain metastasis progression was dynamically monitored using an in vivo bioluminescence imaging system. Histological staining of brain sections confirmed the formation of brain metastases and the distribution of astrocytes and microglia surrounding the tumor (Fig. 1C). Bioluminescence imaging results showed that, compared with the control group, the irradiated group exhibited a significantly increased bioluminescence signal intensity of brain metastases (as early as day 3 post-injection),

indicating reduced barrier function and more rapid progression in irradiated mice (Fig. 1E, G). Survival analysis demonstrated that the median survival time of the irradiated group was significantly shortened (Fig. 1F). The irradiated group also showed a faster body weight loss during the experimental period (Fig. 1H). Collectively, these results indicate that the internal carotid artery injection method successfully establishes a mouse model of breast cancer brain metastasis, and that brain irradiation significantly promotes brain metastasis progression and shortens the survival of irradiated group.

Collectively, mice in the irradiated group showed significantly worse overall survival and increased late-stage metastatic burden, suggesting that brain irradiation may affect the colonization and growth of tumor cells in the brain starting from the early stage.

1. **A.** Experimental timeline of the animal study.
2. **B.** Schematic diagram of brain irradiation in mice at a dose of 10 Gy.
3. **C.** Representative histological images of brain tissue sections from the brain metastasis model.
4. **D.** Schematic illustration of the surgical procedure for brain metastasis model establishment via internal carotid artery injection.
5. **E.** Representative bioluminescence images showing brain metastasis progression in 4T1-luc-bearing mice from different treatment groups (control vs. irradiated, n = 5 per group).
6. **F.** Kaplan–Meier survival curves comparing overall survival between control and irradiated mice after 4T1-luc cell inoculation (n = 6 per cohort, P = 0.0003).
7. **G.** Quantitative analysis of bioluminescence signals from brain metastases in control and irradiated mice following 4T1-luc cell injection (n = 5 per group, P = 0.0067).
8. **H.** Body weight changes monitored in control and irradiated mice after 4T1-luc cell inoculation (n = 5 per group, P = 0.004).

All experiments were independently repeated three times. Data are presented as mean ± standard deviation (SD). *P < 0.05, **P < 0.01, ***P < 0.001.

3.2 Normal Brain Irradiation Promotes Early Brain Colonization and Progression of Breast Cancer Metastases

To further validate the effect of brain irradiation on the development of breast cancer brain metastasis (BCBM), we focused on the critical time point of day 7 post-inoculation and performed pathological staining of mouse brain sections to quantify the number of metastatic foci. In vivo bioluminescence imaging showed that the irradiated group exhibited a significantly increased bioluminescence signal intensity of brain metastases compared with the control group at day 7 post-inoculation (Fig. 2A-B), along with reduced body weight (Fig. 2C). H&E staining of brain tissues and quantitative analysis revealed that the number of brain metastatic foci was significantly increased in the irradiated group (Fig. 2D-E). Ki-67 immunohistochemical staining further demonstrated a significant increase in the number of metastatic foci in the irradiated group (Fig. 2F-G). Collectively, these results further indicate that brain irradiation promotes the early colonization of breast cancer brain metastasis and accelerates the invasion and progression of brain metastases.

A-C. Representative bioluminescence images of brain metastases (A), quantitative analysis of signal intensity (B) (n = 3 per group, P = 0.0313), and body weight changes (C) (n = 8, P = 0.0031) in control versus irradiated mice on day 7 post-carotid artery injection.

D-E. Representative H&E-stained brain tissue images (D) and quantitative analysis of metastatic foci number (E) (n = 4 per group, P = 0.0169). Scale bar: 25 um.

F-G. Representative staining images (F) and quantification of metastatic lesions (G) (n = 4 per group, P = 0.0102). Scale bars: 200 um (left), 50 um (middle), and 25 um (right).

All experiments were independently repeated three times. Data are presented as mean ± SD. *P < 0.05, **P < 0.01, ***P < 0.001.

3.3 Normal Brain Irradiation Increased BBB Leakage and Downregulation of Tight Junction Proteins

Previous studies have shown that brain irradiation induces disruption of the blood-brain barrier (BBB) in the brain, leading to radiation-induced brain injury.[21] Given that brain irradiation promoted tumor cell colonization as early as the initial stage of brain metastasis, we hypothesized that it might facilitate tumor cell crossing of the vascular barrier by disrupting blood-brain barrier (BBB) integrity. To test this hypothesis, we assessed BBB integrity in mouse brain tissues. FITC-dextran leakage assays and immunofluorescence staining revealed a significantly increased FITC-dextran leakage signal in the brain tissues of the irradiated group (Fig. 3A-B), indicating elevated BBB permeability. CD31 immunofluorescence staining showed a marked increase in perivascular fluorescence leakage signals in the irradiated group (Fig. 3C-D), further suggesting enhanced vascular permeability. Co-localization analysis of fibrinogen and CD31 demonstrated obvious fibrinogen leakage into the brain parenchyma of irradiated mice, indicating impaired vascular barrier function (Fig. 3E-F). Western blot analysis further revealed significant downregulation of the tight junction proteins ZO-1, VE-Cad, Occludin, and Claudin-5 in the brain tissues of the irradiated group (Fig. 3G-H). Immunofluorescence staining also confirmed that the ZO-1 fluorescence signal was markedly attenuated and exhibited a discontinuous distribution in brain sections of irradiated mice (Fig. 3I-J). Collectively, these results suggest that brain irradiation disrupts the structural integrity of cerebral vessels by downregulating tight junction protein expression, thereby inducing increased BBB permeability.

A-B. Representative fluorescence images and quantitative analysis of FITC-dextran leakage in brain tissues from different treatment groups. Scale bar: 50 um.

C-D. Representative immunofluorescence staining images and quantitative analysis of CD31 in mouse brain tissues (n = 3 per group, P = 0.0011). Scale bar: 10 um.

E-F. Representative double immunofluorescence staining images and quantitative analysis of Fibrinogen and CD31 in mouse brain tissues (n = 4 per group, P = 0.0033). Scale bar: 10 um.

G-H. Western blotting detection and quantitative analysis of BBB-related tight junction protein expression levels in brain tissues from different treatment groups (n = 3 per group, ZO-1, P = 0.0064; VE-Cad, P = 0.0291; Occludin, P = 0.0083; Claudin5, P = 0.0056).

I-J. Representative immunofluorescence staining images and quantitative analysis of ZO-1 in mouse brain tissues (n = 3 per group, P = 0.011). Scale bar: 50 um.

All experiments were independently repeated three times. Data are presented as mean ± standard deviation (SD). *P < 0.05, **P < 0.01, ***P < 0.001.

3.4 Irradiated Astrocytes Promote Breast Cancer Cell Migration, Invasion, and Proliferation

Astrocytes are the most abundant cell type in the brain and serve as important structural supports for the blood–brain barrier (BBB).[22] In the brain tumor microenvironment, astrocytes and cancer cells can interact through gap junctions, and through the release of factors like TNF-α and IFN-γ, astrocytes can facilitate the progression of tumors.[11a] To explore the cellular mechanisms underlying the above in vivo findings, an in vitro co-culture system of C8D1A astrocytes and 4T1 breast cancer cells was established to simulate cell-cell interactions in the brain metastatic microenvironment. To determine the optimal irradiation dose for astrocytes in the experimental group, a series of preliminary experiments were performed, and a dose of 4 Gy was selected for the irradiated group (Fig. S1). Transwell assay results demonstrated that co-culture with irradiated astrocytes significantly enhanced the migration (through uncoated membranes) and Matrigel-based invasion abilities of 4T1 cells. (Fig. 4A-C). Wound healing assays further confirmed that the migration rate of 4T1 cells was markedly accelerated after co-culture with irradiated astrocytes (Fig. 4D-E). Colony formation assays and CCK-8 proliferation assays demonstrated that irradiated astrocytes significantly promoted the colony-forming ability and proliferative viability of 4T1 cells (Fig. 4F-H). In contrast, Annexin V-FITC flow cytometry revealed no significant change in the apoptosis rate of 4T1 cells in the co-culture system (Supplementary Figure). Collectively, these results indicate that irradiated astrocytes specifically enhance the migration, invasion, and proliferation abilities of 4T1 cells, with no significant effect on apoptosis.

Figure 4 Irradiated Astrocytes Promote Breast Cancer Cell Migration, Invasion, and Proliferation

A-C. Transwell migration and invasion assays assessing the effects of irradiated astrocytes on the migratory and invasive capacities of 4T1 cells. Representative images (A) and quantitative analyses (B, C), n = 3 per group. Migration: P ≤ 0.001; Invasion: Ctrl vs. IR P < 0.001, Mock-IR vs. IR P = 0.002. Scale bar: 25 um.

D-E. Wound healing assay evaluating the migration ability of 4T1 cells after co-culture. Representative images (D) and quantitative analysis (E), n = 3 per group. Ctrl vs. IR P = 0.001, Mock-IR vs. IR P = 0.0159. Scale bar: 100 um.

F-G. Colony formation assay detecting the proliferative capacity of 4T1 cells. Representative images (F) and quantitative analysis (G), n = 3 per group. Ctrl vs. Mock-IR P = 0.1581; Ctrl vs. IR P = 0.0028; Mock-IR vs. IR P = 0.0253.

H. CCK-8 proliferation assay measuring the viability of 4T1 cells at different co-culture time points, with quantitative analyses for each time point, n = 3 per group, Mock-IR vs. IR P < 0.001.

All experiments were independently repeated three times. Data are presented as mean ± standard deviation (SD). *P < 0.05, **P < 0.01, ***P < 0.001.

3.5 Secreted Factors from Irradiated Astrocyte-Breast Cancer Cell Co-Cultures Disrupt Endothelial Barrier Integrity

Given the observed disruption of the blood–brain barrier (BBB) in vivo and the regulatory effects of astrocytes on tumor cells described above, we further investigated whether the interaction between astrocytes and breast cancer cells affects endothelial barrier function through paracrine mechanisms, continuing to simulate cell-cell interactions in the brain metastatic microenvironment. First, a direct contact co-culture system of C8D1A and GFP-4T1 cells was established (Fig. 5A), and the two cell populations were successfully sorted by flow cytometry (Fig. 5B). RT-PCR and ELISA results showed that the mRNA and protein levels of multiple secreted factors, including VEGF, IFN-γ, TNF-α, and TGFβ, were significantly upregulated in irradiated astrocytes and in the supernatants of the post-irradiation co-culture system (Fig. 5C-D). An in vitro BBB model was established using bEnd.3 cells (Fig. 5E). The FITC-dextran permeability assay revealed that stimulation with supernatants from the post-irradiation co-culture system significantly increased the permeability of the bEnd.3 monolayer barrier (Fig. 5F). Western blot analysis showed that the expression levels of tight junction proteins were markedly downregulated in bEnd.3 cells in this treatment group (Fig. 5G). KEGG pathway enrichment analysis of transcriptome sequencing data suggested that these changes might be associated with regulation of the VEGF signaling pathway (Fig. 5H-I). Collectively, these results indicate that the post-irradiation co-culture system of astrocytes and breast cancer cells stimulates endothelial cells through the secretion of inflammatory factors (such as TNF-α and IFN-γ) and growth factors (such as VEGF and TGFβ), as well as regulation of the VEGF signaling pathway, thereby inducing downregulation of tight junction proteins and increased BBB permeability. **Figure 5 Secreted Factors from Irradiated Astrocyte-Breast Cancer Cell Co-Cultures Disrupt Endothelial Barrier Integrity**

1. **A.** Schematic diagram of the direct contact co-culture model between C8D1A and GFP-4T1 cells.
2. **B.** Flow cytometry gating strategy following direct co-culture, showing cell population distribution. The P3 gate represents 4T1 cells, and the P4 gate represents C8D1A cells.

3. **C.** RT-PCR analysis of mRNA expression levels of secretory factors in astrocytes before and after irradiation (n = 3 per group, P<0.001).
4. **D.** ELISA detection of protein expression levels of secretory factors in the supernatant of the co-culture system (n>3 per group, P<0.001).
5. **E.** Schematic illustration of the *in vitro* blood–brain barrier permeability assay using bEnd.3 cells.
6. **F.** Quantitative analysis of FITC-dextran permeability assay showing changes in bEnd.3 monolayer barrier permeability across different treatment groups (n = 6 per group, P<0.001).
7. **G.** Western blotting detection of changes in tight junction protein expression levels in bEnd.3 cells.
8. **H.** KEGG pathway enrichment analysis based on transcriptome sequencing of bEnd.3 cells from different treatment groups.

1. **I.** Downregulation of the VEGF pathway in bEnd.3 cells following co-culture with irradiated astrocytes.

All experiments were independently repeated three times. Data are presented as mean ± standard deviation (SD). *P < 0.05, **P < 0.01, ***P < 0.001.

3.6 Normal Brain Irradiation Induces Astrocyte Senescence In Vivo and In Vitro

The above in vitro experiments clearly demonstrated the dual regulatory effects of irradiated astrocytes on both tumor cells and endothelial cells, suggesting that astrocytes themselves may undergo key phenotypic changes. To further investigate the molecular characteristics of astrocytes following irradiation, transcriptome sequencing analysis was performed. Compared with the control group, the irradiated group showed significant enrichment of senescence-related Gene Ontology (GO) biological processes and Kyoto Encyclopedia of Genes and Genomes (KEGG) pathways in astrocytes (Fig. 6A-D). SA-β-Gal staining revealed that the percentage of senescent cells was significantly increased in both brain tissues and astrocyte cell lines from the irradiated group (Fig. 6E-G). p16 immunofluorescence staining further confirmed that the p16-positive signal was higher in the brain tissues of the irradiated group and was predominantly localized in GFAP-labeled astrocytes (Fig. 6H-I). Western blot analysis showed that the expression levels of p21 was significantly upregulated in the brain tissues of the irradiated group (Fig. 6J). Meanwhile, γH2AX immunofluorescence staining demonstrated a significantly enhanced DNA damage signal in the brain tissues of the irradiated group (Fig. 6K-L). Collectively, these results indicate that brain irradiation induces a senescent phenotype in astrocytes, accompanied by accumulation of DNA damage and upregulation of senescence-related markers.

Figure 6 Normal Brain Irradiation Induces Astrocyte Senescence In Vivo and In Vitro

A-B. Transcriptome sequencing analysis of astrocytes in the control versus irradiated groups: Top 20 upregulated GO biological processes (A) and KEGG pathway enrichment analysis (B) (n = 3 per group).

C-D. Cellular senescence-related pathways were significantly upregulated in both GO (C) and KEGG (D) enrichment analyses.

E. Representative images of SA-β-Gal senescence staining in mouse brain tissue (n = 3 per group). Scale bars: 100 um (left) and 25 um (right).

F-G. Representative images of SA-β-Gal senescence staining in mouse astrocytes (F) and quantitative analysis of the percentage of positive cells (G) (n = 3 per group, P = 0.0013). Scale bar: 25 um.

H-I. Representative double immunofluorescence staining images of GFAP and p16 in mouse brain tissue (H) and quantitative analysis (I) (n = 4 per group, P = 0.0039). Scale bar: 25 um.

J. Western blotting detection of senescence-associated protein levels (p21) in brain tissues from different treatment groups.

K-L. Representative immunofluorescence staining images and quantitative analysis of γH2AX in mouse brain tissue, reflecting DNA damage levels (n = 5 per group, P<0.001). Scale bar: 25 um.

All experiments were independently repeated three times. Data are presented as mean ± standard deviation (SD). *P < 0.05, **P < 0.01, ***P < 0.001.

3.7 Senescent Astrocyte-Derived HGF Activates

c-Met/PI3K/AKT Signaling and Promotes Breast Cancer Cell Migration and Invasion

Based on the finding of astrocyte senescence, we further investigated the molecular mechanisms by which senescent astrocytes mediate the malignant phenotype of tumor cells. Immunofluorescence staining revealed a clear spatial co-localization of GFAP-labeled astrocytes and IBA1-labeled microglia surrounding metastatic foci in brain tissues of mice with brain metastasis (Fig. 7A). Principal component analysis (PCA) of transcriptome sequencing data showed a distinct gene expression profile between the irradiated and control groups of astrocytes (Fig. 7B). Further analysis revealed significant upregulation of senescence-associated secretory phenotype (SASP) gene expression in the irradiated group (Fig. 7C). To identify key effector molecules within the SASP, we focused on HGF and found that both its mRNA and protein secretion levels were significantly elevated following irradiation (Fig. 5C, 7D). To verify the effect of HGF derived from senescent astrocytes on signaling pathways in breast cancer cells, we examined the activation of c-Met (the receptor of HGF) and its downstream PI3K/AKT pathway in 4T1 cells. Western blot analysis showed that in 4T1 cells co-cultured with irradiated astrocytes, the phosphorylation level of c-Met was significantly enhanced, and the phosphorylation levels of downstream PI3K and AKT were also markedly upregulated (Fig. 7E-G). To further validate the promoting effect of HGF on the malignant phenotype of tumor cells, in vitro experiments were performed using an HGF-neutralizing antibody (R&D Systems, Catalog No. AF2207, 1 ug/mL). The results demonstrated that the co-culture system of irradiated astrocytes promoted breast cancer cell migration and invasion, whereas depletion of HGF inhibited this effect (Fig. 7H-I). Collectively, these results indicate that

irradiation induces astrocyte senescence, and that senescent astrocytes activate the c-Met/PI3K/AKT signaling pathway in breast cancer cells through the secretion of HGF, thereby promoting tumor cell migration and invasion.

Figure7Senescent Astrocyte-Derived HGF Activates c-Met/PI3K/AKT Signaling and Promotes Breast Cancer Cell Migration and Invasion

A. Representative immunofluorescence co-localization images of tumor cells with GFAP and IBA1 in brain tissue sections from mice with brain metastases. Scale bar: 25 um (n = 3 per group).

B-C. Principal component analysis (PCA) of transcriptome sequencing data from mouse astrocytes (B) and analysis of differentially expressed genes related to the senescence-associated secretory phenotype (SASP) (C).

D. ELISA detection of changes in HGF protein secretion levels in the supernatant of the co-culture system (n = 3 per group, P<0.001).

E-G. Western blotting detection of changes and quantitative analysis in the expression levels of c-Met, PI3K, AKT, and their phosphorylated proteins in breast cancer cells from different treatment groups (n = 3 per group, P-c-Met: P = 0.0038; P-PI3K: P<0.001; P-AKT: P<0.001).

H-I. Representative images and quantitative analysis of Transwell migration and invasion assays of 4T1 cells after co-culture with anti-HGF neutralizing antibody *in vitro* (n = 3 per group, Migration: Mock-IR vs. IR P = 0.0018, IR vs. anti-HGF P = 0.004; Invasion: Mock-IR vs. IR P = 0.003, IR vs. anti-HGF P = 0.0023).

All experiments were independently repeated three times. Data are presented as mean ± standard deviation (SD). *P < 0.05, **P < 0.01, ***P < 0.001.

3.8 Clearance of Senescent Astrocytes Attenuates the Pro-Metastatic Effects of Normal Brain Irradiation and Inhibits BCBM Progression

To further functionally validate the direct role of astrocyte senescence in brain irradiation-promoted breast cancer brain metastasis (BCBM), in vivo rescue experiments were performed using the senolytic agent ABT-263 (Fig. 8A). In vivo bioluminescence imaging showed that as early as day 2 post-inoculation, the brain metastatic signal was significantly enhanced in the irradiated group, whereas co-treatment with ABT-263 effectively suppressed this effect (Fig. 8B-C), suggesting that elimination of senescent astrocytes inhibits early tumor cell penetration of the blood–brain barrier and colonization within the brain. During the tumor-bearing period, the brain metastatic signal in the irradiated group further increased, while the ABT-263 co-treatment group maintained a lower metastatic burden (Fig. 8D-G). Survival analysis further demonstrated that ABT-263 significantly prolonged the median survival of mice in the irradiated group (Fig. 8H). Body weight monitoring showed that the irradiated group exhibited the most rapid body weight loss during the tumor-bearing period, and this effect was ameliorated by ABT-263 treatment (Fig. 8I). Collectively, these results indicate that elimination of senescent astrocytes

effectively blocks brain irradiation-induced early blood–brain barrier penetration and subsequent brain metastasis progression, further confirming that astrocyte senescence is a key driver of post-radiotherapy brain metastasis.

Figure 8 Clearance of Senescent Astrocytes Attenuates the Pro-Metastatic Effects of Normal Brain Irradiation and Inhibits BCBM Progression

A. Experimental flowchart of the *in vivo* rescue study.

B-C. Representative bioluminescence images (B) and quantitative analysis of photon flux (C) monitoring brain metastasis progression on day 2 after internal carotid artery inoculation of 4T1-luc cells in different treatment groups (n = 5 per group, 0GY vs. 10GY P<0.0001, 10GY vs. ABT-263 P<0.0001).

D. Representative bioluminescence images monitoring brain metastasis progression on day 7 after internal carotid artery inoculation of 4T1-luc cells in different treatment groups.

E-G. Quantitative analysis of bioluminescence signals from brain metastases after inoculation of 4T1-luc cells in different groups (n = 5 per group, 0GY vs. 10GY P<0.0001, 10GY vs. ABT-263 P<0.0001).

1. **H.** Kaplan–Meier survival curves comparing overall survival among different treatment groups after 4T1-luc cell inoculation (n = 5 per cohort, 0GY vs. 10GY P = 0.0025, 10GY vs. ABT-263 P = 0.0025).

1. **I.** Body weight changes monitored in different treatment groups after 4T1-luc cell inoculation (n = 5 per group, 0GY vs. 10GY P = 0.0113, 10GY vs. ABT-263 P = 0.003).

All experiments were independently repeated three times. Data are presented as mean ± standard deviation (SD). *P < 0.05, **P < 0.01, ***P < 0.001.

4. Discussion

Breast cancer brain metastasis (BCBM) represents a formidable challenge in clinical practice. Although whole-brain radiotherapy (WBRT) remains an important palliative treatment modality, its efficacy is limited and it may be associated with potential risks such as cognitive impairment.[23] However, whether radiotherapy might inadvertently exacerbate tumor progression through remodeling of the brain metastatic microenvironment (BMM) has long been underappreciated.[24] In this study, we observed that brain irradiation significantly promoted the early colonization of breast cancer cells in the brain and the progression of metastatic lesions. This finding is highly consistent with recent preclinical studies demonstrating the "double-edged sword" effect of radiotherapy.[8, 10, 25] Notably, we further revealed that this pro-metastatic effect was not mediated by a direct action on tumor cells, but primarily through the induction of a senescent phenotype in astrocytes, a key component of the brain microenvironment. These results suggest that whole-brain or large-field local irradiation alone may be insufficient to control brain metastases and might even exert potential long-term detrimental effects through unfavorable microenvironmental remodeling, a phenomenon also referred to as the "abscopal effect".[7, 10]

It is well established that astrocytes, as the predominant glial cells in the CNS, are essential for preserving BBB structural integrity and for sustaining the homeostatic balance of the neural microenvironment.[26] Recent studies have demonstrated that ionizing radiation (IR) effectively induces astrocytes to enter a senescent state and activates their senescence-associated secretory phenotype (SASP).[12] Building upon these findings, the present study established, for the first time, a direct causal link between IR-induced astrocyte senescence and BCBM progression, using in vivo and in vitro functional assays, molecular biological analyses, and transcriptome sequencing. We not only validated the promoting effects of IR on metastatic tumor growth and cancer cell invasion in a mouse brain metastasis model and an in vitro co-culture system, but also confirmed, at both histological and molecular levels, the senescent phenotype of astrocytes following irradiation and the significant enrichment of SASP pathway-related genes. Through mechanistic dissection, we further identified hepatocyte growth factor (HGF) as a key effector molecule within the SASP of senescent astrocytes. HGF activated the c-Met receptor on breast cancer cells and its downstream PI3K/AKT signaling pathway, thereby enhancing the malignant phenotype of tumor cells. This finding is consistent with studies demonstrating the role of the HGF/c-Met signaling axis in various types of tumor metastasis;[9a, 27] however, the present study provides the first evidence, specifically in the context of breast cancer brain metastasis, that senescent astrocytes represent a critical and previously overlooked source of aberrant activation of this signaling axis.

Another key finding of this study is that brain irradiation disrupted the structural integrity of the BBB by inducing astrocyte senescence. The BBB is the most critical barrier limiting the colonization of circulating tumor cells in the brain, and its function depends on the normal expression and proper localization of tight junction proteins (such as ZO-1 and Occludin) in brain microvascular endothelial cells.[28] Our results demonstrated that SASP factors secreted by irradiated astrocytes significantly downregulated the expression of junction proteins in bEnd.3 cells, thereby increasing BBB permeability. This finding is consistent with previous studies showing that SASP factors (such as IL-6 and VEGF) disrupt vascular barrier function,[29] and for the first time, functionally links astrocyte senescence, BBB dysfunction, and BCBM progression into a cohesive cascade. Integrating dynamic observations of early brain metastatic colonization, we propose that SASP-mediated BBB disruption may be a critical prerequisite for successful tumor cell colonization in the brain, and that irradiation-induced astrocyte senescence serves as a key upstream event driving this process.

Given these findings, we reasoned that if astrocyte senescence is a core driver of IR-promoted brain metastasis, then targeted elimination of these senescent cells should block this effect. This hypothesis was tested through in vivo rescue experiments employing ABT-263, a senolytic agent and Bcl-2 family inhibitor that selectively triggers apoptosis in senescent cells.[30] The results were highly consistent with our hypothesis: elimination of senescent astrocytes not only effectively inhibited IR-induced early BBB penetration but also significantly delayed brain metastasis progression and prolonged the survival of BCBM mice. This finding is consistent with previous conclusions regarding the role of senescence in glioma.[9a] This series of functional rescue experiments causally solidifies the key role of astrocyte senescence in IR-promoted brain metastasis.[31] In recent years, senolytics have shown promising

therapeutic potential in various aging-related diseases.[30b, 32] The present study extends their application to the field of radiotherapy-associated brain metastasis, strongly suggesting that combining radiotherapy with senolytics (ABT-263) may represent a novel strategy to optimize radiotherapy for breast cancer brain metastasis and mitigate its "double-edged sword" effect.

This study has several limitations that warrant further investigation. First, although we identified HGF as a key molecule within the SASP of senescent astrocytes through in vitro experiments, the SASP components are highly dynamic and cell type-dependent.[7] Whether additional synergistic factors (such as IL-6 or CXCL12) cooperatively act on tumor cells or endothelial cells requires systematic identification through multi-factor neutralization or gene knockout experiments. Second, this study was primarily conducted using the triple-negative breast cancer cell line 4T1; the generalizability of these findings to other breast cancer subtypes (such as hormone receptor-positive or HER2-positive) remains to be validated. Third, the molecular details linking astrocyte senescence to BBB disruption are still not fully understood: which specific SASP factors directly act on tight junction proteins of endothelial cells, and what are their downstream signaling pathways? These questions need to be precisely addressed through targeted neutralizing antibodies or conditional gene knockout mice. Fourth, the brain metastasis model used in this study, established by internal carotid artery injection, effectively simulates the late stage of hematogenous metastasis but does not fully recapitulate the entire process of tumor cell detachment from the primary site, entry into the circulation, and subsequent crossing of the BBB. Future studies incorporating spontaneous metastasis models will further enhance the clinical relevance of the conclusions. Finally, from a clinical translational perspective, the potential toxicity of senolytic agents such as ABT-263, particularly dose-limiting thrombocytopenia, may be poorly tolerated in patients with brain metastases. Regarding future directions, the timing and sequence of low-dose radiotherapy combined with senolytics should be systematically optimized, and other key SASP factors (such as IL-6, CXCL1) merit screening as potential co-targets to suppress tumor invasion and BBB disruption.

5. Conclusions

In summary, this study demonstrates that irradiation of normal brain tissue can establish a pro-metastatic microenvironment that facilitates breast cancer brain colonization and progression. Astrocyte senescence serves as a key upstream event linking cranial irradiation to brain metastasis. Senescent astrocytes promote metastasis through two complementary mechanisms. They compromise blood-brain barrier integrity through senescence-associated secretory responses, thereby facilitating early tumor cell colonization. In parallel, astrocyte-derived HGF activates c-Met/PI3K/AKT signaling in breast cancer cells, enhancing their migration, invasion, and proliferation. Clearance of senescent astrocytes with ABT-263 attenuates blood-brain barrier leakage and brain metastatic progression and prolongs survival, supporting the causal contribution of astrocyte senescence to the pro-metastatic effects of irradiation. These findings provide a mechanistic framework for understanding how normal brain irradiation shapes a microenvironment permissive for breast cancer brain metastasis. They also identify senescent astrocytes as a potential therapeutic target, although the clinical value of senolytic intervention requires further investigation.

Declarations

Ethics approval and consent to participate

The study has been approved by the Institutional Animal Care and Use Committee (IACUC) of the Animal Experiment Center of Wuhan University (approval No. 210971413).

Consent for publication

Not applicable.

Availability of data and materials

The snRNA-seq data generated and analyzed in this study will be publicly available in the NCBI GEO repository under accession code XXXX upon publication.

Conflict of Interest

The authors declare no conflict of interest.

Funding

This study was supported by grants from the National Natural Science Foundation of China (No. 82073349), the Department of Science and Technology of Hubei Province Natural Science Foundation Innovative Development Joint Fund (No. 2024AFD426), the Science and Technology Innovation Cultivation Fund of Zhongnan Hospital, Wuhan University (No. CXPY2023049), the Natural Science Foundation of Hubei Province (No. 2024AFB799), and the Hubei Provincial Administration of Traditional Chinese Medicine (No. ZYYCC2023002).

Author Contributions

Shiyu Cheng: conceptualization and design, methodology development, data curation and analysis, writing of the original draft, formal analysis, figure preparation, and experimental operations. Yuan Ke, Linhui Zheng, Jingtian Yu, Gong Zhang, Zhiyuan Xiong, Yue Liu, Wanyu Chen, Dong Liu, Yue Liu: experimental operations. Haijun Yu and Chaoyan Wu: project supervision, funding acquisition, manuscript review and editing, and final approval of the manuscript. All authors have read and agreed to the publication of the final manuscript.

Supporting information

Supplementary Materials and Methods.

Supplementary Figures.

Acknowledgements

Not available.

Contributor Information

Shiyu Cheng, E-mail: 2173683037@qq.com;

Yuan Ke, E-mail: Keyuan0912@163.com;

Linhui Zheng, E-mail: 2021283030233@whu.edu.cn;

Jingtian Yu, E-mail: jingtian_yu@whu.edu.cn

Gong Zhang, E-mail: zhanggong01@163.com

Zhiyuan Xiong, E-mail: 2020305232104@whu.edu.cn

Yue Liu, E-mail: junely00@163.com

Wanyu Chen, E-mail: 13623027627@163.com

Dong Liu, E-mail: 2023203030041@whu.edu.cn

Chaoyan Wu, E-mail: grace98765@163.com

Haijun Yu, E-mail: haijunyu@whu.edu.cn.

Data Availability Statement

The data supporting the findings of this study are publicly available in the [Database Name] repository under reference number [XXXX].

Generative AI and AI-assisted technologies were NOT used in the preparation of this work.

References

1. a) F, Bray M, Laversanne H, Sung J, Ferlay RL, Siegel I, Soerjomataram A, Jemal CACJC. 2024, *74*(3), 229. https://doi.org/10.3322/caac.21834; b) J. Kim, A. Harper, V. McCormack, H. Sung, N. Houssami, E. Morgan, M. Mutebi, G. Garvey, I. Soerjomataram, M. M. Fidler-Benaoudia, *Nat Med* 2025, *31*(4), 1154, https://doi.org/10.1038/s41591-025-03502-3.
2. Boire A, Brastianos PK, Garzia L, Valiente M. Nat Rev Cancer. 2020;20(1):4. https://doi.org/10.1038/s41568-019-0220-y.
3. Pardridge WM. *NeuroRx* 2005, *2*(1), 3. https://doi.org/10.1602/neurorx.2.1.3

4. Nguyen B, Fong C, Luthra A, Smith SA, DiNatale RG, Nandakumar S, Walch H, Chatila WK, Madupuri R, Kundra R, Bielski CM, Mastrogiacomo B, Donoghue MTA, Boire A, Chandarlapaty S, Ganesh K, Harding JJ, Iacobuzio-Donahue CA, Razavi P, Reznik E, Rudin CM, Zamarin D, Abida W, Abou-Alfa GK, Aghajanian C, Cercek A, Chi P, Feldman D, Ho AL, Iyer G, Janjigian YY, Morris M, Motzer RJ, O'Reilly EM, Postow MA, Raj NP, Riely GJ, Robson ME, Rosenberg JE, Safonov A, Shoushtari AN, Tap W, Teo MY, Varghese AM, Voss M, Yaeger R, Zauderer MG, Abu-Rustum N, Garcia-Aguilar J, Bochner B, Hakimi A, Jarnagin WR, Jones DR, Molena D, Morris L, Rios-Doria E, Russo P, Singer S, Strong VE, Chakravarty D, Ellenson LH, Gopalan A, Reis-Filho JS, Weigelt B, Ladanyi M, Gonen M, Shah SP, Massague J, Gao J, Zehir A, Berger MF, Solit DB, Bakhoum SF. F. Sanchez-Vega, N. Schultz, *Cell* 2022, *185*(3), 563. https://doi.org/10.1016/j.cell.2022.01.003
5. a) B, Tomasik M, Bieńkowski Z, Górska K, Gutowska P, Kumięga J, Jassem R, Duchnowska. 2023, *114*, 102521. https://doi.org/10.1016/j.ctrv.2023.102521; b) M. Ivanova, F. M. Porta, F. Giugliano, C. Frascarelli, E. Sajjadi, K. Venetis, G. Cursano, G. Mazzarol, E. Guerini-Rocco, G. Curigliano, C. Criscitiello, N. Fusco, *Genes (Basel)* 2023, *14*(6), https://doi.org/10.3390/genes14061160.
6. a) M, Hosonaga H, Saya Y, Arima. 2020, *39*(3), 711. https://doi.org/10.1007/s10555-020-09881-y; b) M. Benjamin, P. Malakar, R. A. Sinha, M. W. Nasser, S. K. Batra, J. A. Siddiqui, B. Chakravarti, *Adv Cancer Biol Metastasis* 2023, *7*, 100079, https://doi.org/10.1016/j.adcanc.2022.100079.
7. Schiff D, Messersmith H, Brastianos PK, Brown PD, Burri S, Dunn IF, Gaspar LE, Gondi V, Jordan JT, Maues J, Mohile N, Redjal N, Stevens GHJ, Sulman EP, van den Bent M, Wallace HJ, Zadeh G, Vogelbaum MA. J Clin Oncol. 2022;40(20):2271. https://doi.org/10.1200/jco.22.00333.
8. Wang M, Xu L, Alu A, Li P, Liu J, Chen S, He X, Han X, Yang L, Pu Q, Wei X. Signal Transduct Target Ther. 2025;10(1):391. https://doi.org/10.1038/s41392-025-02471-w.
9. a) E, Fletcher-Sananikone S, Kanji N, Tomimatsu LFM, Di Cristofaro RK, Kollipara D, Saha JR, Floyd P, Sung R, Hromas TC, Burns R, Kittler AA, Habib B, Mukherjee S, Burma, Feng Y, Hu X, Zhang Y, Wang Y. 2021, *81*(23), 5935. https://doi.org/10.1158/0008-5472.Can-21-0752; b) M. A. Shumakovich, C. P. Mencio, J. S. Siglin, R. A. Moriarty, H. M. Geller, K. M. Stroka, *Faseb j* 2017, *31*(11), 5049, https://doi.org/10.1096/fj.201700254R; c) Y. Feng, X. Hu, Y. Zhang, Y. Wang *Aging Dis* 2023, https://doi.org/10.14336/ad.2023.0514.
10. Piffko A, Yang K, Panda A, Heide J, Tesak K, Wen C, Zawieracz K, Wang L, Naccasha EZ, Bugno J, Fu Y, Chen D, Donle L, Lengyel E, Tilley DG, Mack M, Rock RS, Chmura SJ, Vokes EE, He C, Pitroda SP, Liang HL, Weichselbaum RR. Nature. 2025;643(8072):810. https://doi.org/10.1038/s41586-025-08994-0.
11. a) Q, Chen A, Boire X, Jin M, Valiente EE, Er A, Lopez-Soto L, Jacob R, Patwa H, Shah K, Xu JR, Cross J, Massagué. *Nature* 2016, *533*(7604), 493. https://doi.org/10.1038/nature18268; b) G. Lorusso, C. B. Wyss, F. Kuonen, N. Vannini, C. Billottet, N. Duffey, R. Pineau, Q. Lan, P. Wirapati, D. Barras, A. Tancredi, R. Lyck, H. A. Lehr, B. Engelhardt, M. Delorenzi, A. Bikfalvi, C. Rüegg, *Sci Transl Med* 2022, *14*(661), eaax8933, https://doi.org/10.1126/scitranslmed.aax8933.
12. a) R, Gulej Á, Nyúl-Tóth C, Ahire J, DelFavero P, Balasubramanian T, Kiss S, Tarantini Z, Benyo P, Pacher B, Csik A, Yabluchanskiy P, Mukli A, Kuan-Celarier IA, Krizbai J, Campisi WE, Sonntag A,

Csiszar Z, Ungvari, Berg TJ, Marques C, Pantazopoulou V, Johansson E, von Stedingk K, Lindgren D, Jeannot P, Pietras EJ, Bergström T, Swartling FJ, Governa V, Bengzon J, Belting M, Axelson H, Squatrito M, Pietras A. 2023, *45*(5), 2983. https://doi.org/10.1007/s11357-023-00870-x; b) C. Turnquist, J. A. Beck, I. Horikawa, I. E. Obiorah, N. Von Muhlinen, B. Vojtesek, D. P. Lane, C. Grunseich, J. J. Chahine, H. M. Ames, D. D. Smart, B. T. Harris, C. C. Harris, *Neuro Oncol* 2019, *21*(4), 474, https://doi.org/10.1093/neuonc/noz001; c) T. J. Berg, C. Marques, V. Pantazopoulou, E. Johansson, K. von Stedingk, D. Lindgren, P. Jeannot, E. J. Pietras, T. Bergström, F. J. Swartling, V. Governa, J. Bengzon, M. Belting, H. Axelson, M. Squatrito, A. Pietras *Cancer Res* 2021, *81*(8), 2101, https://doi.org/10.1158/0008-5472.Can-20-1785.

13. Zhang D, Zhang JW, Xu H, Chen X, Gao Y, Jiang HG, Wang Y, Wu H, Yang L, Wang WB, Dai J, Xia L, Peng J, Zhou FX. Mol Cancer. 2024;23(1):70. https://doi.org/10.1186/s12943-024-01985-1.
14. Yu-Ju Wu C, Chen CH, Lin CY, Feng LY, Lin YC, Wei KC, Huang CY, Fang JY, Chen PY. Neuro Oncol. 2020;22(2):253. https://doi.org/10.1093/neuonc/noz189.
15. Xie Y, Sun Y, Liu Y, Zhao J, Liu Q, Xu J, Qin Y, He R, Yuan F, Wu T, Duan C, Jiang L, Lu H, Hu J. ACS Nano. 2023;17(18):18008. https://doi.org/10.1021/acsnano.3c04423.
16. Ji J, Ding K, Luo T, Zhang X, Chen A, Zhang D, Li G, Thorsen F, Huang B, Li X, Wang J. Cell Death Differ. 2021;28(1):367. https://doi.org/10.1038/s41418-020-00606-w.
17. Godinho-Pereira J, Vaz D, Figueira I, Aniceto-Romão J, Krizbai I, Malhó R, Rocha J, Carvalheiro MC, Simões S, Gaspar MM, Brito MA. Cells. 2023;12(16). https://doi.org/10.3390/cells12162076.
18. Li Y, Liu B, Zhao T, Quan X, Han Y, Cheng Y, Chen Y, Shen X, Zheng Y, Zhao Y. J Nanobiotechnol. 2023;21(1):70. https://doi.org/10.1186/s12951-023-01828-z.
19. Lanz MC, Zatulovskiy E, Swaffer MP, Zhang L, Ilerten I, Zhang S, You DS, Marinov G, McAlpine P, Elias JE, Skotheim JM. Mol Cell. 2022;82(17):3255. https://doi.org/10.1016/j.molcel.2022.07.017.
20. Gan S, Macalinao DG, Shahoei SH, Tian L, Jin X, Basnet H, Bibby C, Muller JT, Atri P, Seffar E, Chatila W, Karacay A, Chanda P, Hadjantonakis AK, Schultz N, Brogi E, Bale TA, Moss NS, Murali R, Pe'er D, Massague J. Cancer Cell. 2024;42(10):1693. https://doi.org/10.1016/j.ccell.2024.08.015.
21. Luo N, Zhu W, Li X, Fu M, Zhang Y, Yang F, Zhang Y, Chen Z, Zhang Q, Peng B, Li Q, Chen X, Liu Y, Hu G, Peng X. Neuro Oncol. 2024;26(12):2288. https://doi.org/10.1093/neuonc/noae153.
22. Diaz-Castro B, Robel S, Mishra A. Annu Rev Neurosci. 2023;46:101. https://doi.org/10.1146/annurev-neuro-091922-031205.
23. a) PD, Brown V, Gondi S, Pugh WA, Tome JS, Wefel TS, Armstrong JA, Bovi C, Robinson A, Konski D, Khuntia D, Grosshans TLS, Benzinger D, Bruner MR, Gilbert D, Roberge V, Kundapur K, Devisetty S, Shah K, Usuki BM, Anderson B, Stea H, Yoon J, Li NN, Laack TJ, Kruser SJ, Chmura W, Shi S, Deshmukh MP, Mehta LA, Kachnic. 2020, *38*(10), 1019. https://doi.org/10.1200/jco.19.02767; b) J. H. Suh, R. Kotecha, S. T. Chao, M. S. Ahluwalia, A. Sahgal, E. L. Chang, *Nat Rev Clin Oncol* 2020, *17*(5), 279, https://doi.org/10.1038/s41571-019-0320-3.
24. Schreurs LD, Vom Stein AF, Jünger ST, Timmer M, Noh KW, Buettner R, Kashkar H, Neuschmelting V, Goldbrunner R, Nguyen PH. Neuro Oncol. 2025;27(1):50. https://doi.org/10.1093/neuonc/noae219.

25. Hou Y, Yang K, Wang L, Wang J, Huang X, Piffkó A, Luo SZ, Yu X, Rao E, Martinez C, Bugno J, Mack M, Vokes EE, Pitroda SP, Chmura SJ, Weichselbaum RR, Liang HL. *Clin Cancer Res* 2024, *30*(9), 1945. https://doi.org/10.1158/1078-0432.Ccr-23-3206
26. a) UH, Langen S, Ayloo C, Gu ARCDB. 2019, *35*, 591. https://doi.org/10.1146/annurev-cellbio-100617-062608; b) N. Priego, L. Zhu, C. Monteiro, M. Mulders, D. Wasilewski, W. Bindeman, L. Doglio, L. Martínez, E. Martínez-Saez, Y. C. S. Ramón, D. Megías, E. Hernández-Encinas, C. Blanco-Aparicio, L. Martínez, E. Zarzuela, J. Muñoz, C. Fustero-Torre, E. Piñeiro-Yáñez, A. Hernández-Laín, L. Bertero, V. Poli, M. Sanchez-Martinez, J. A. Menendez, R. Soffietti, J. Bosch-Barrera, M. Valiente, *Nat Med* 2018, *24*(7), 1024, https://doi.org/10.1038/s41591-018-0044-4.
27. a) H, Tao H, Liu H, Zhang H, Ren B, Wen J, Zhang J, Du Z, Cai Z, Deng. 2025, *14*(15), e2405056. https://doi.org/10.1002/adhm.202405056; b) R. Sharma, R. Malviya, *Biochim Biophys Acta Rev Cancer* 2023, *1878*(3), 188869, https://doi.org/10.1016/j.bbcan.2023.188869
28. a) C, Wei W, Jiang R, Wang H, Zhong H, He X, Gao S, Zhong F, Yu Q, Guo L, Zhang LDJ, Schiffelers B, Zhou M, Trepel FI, Schmidt M, Luo F, Shao. 2024, *629*(8013), 893. https://doi.org/10.1038/s41586-024-07314-2; b) S. Dithmer, I. E. Blasig, P. A. Fraser, Z. Qin, R. F. Haseloff, *Int J Mol Sci* 2024, *25*(11), https://doi.org/10.3390/ijms25115601.
29. Zhan R, Meng X, Tian D, Xu J, Cui H, Yang J, Xu Y, Shi M, Xue J, Yu W, Hu G, Li K, Ge X, Zhang Q, Zhao M, Du J, Guo X, Xu W, Gao Y, Yao C, Chen F, Chen Y, Shan W, Zhu Y, Ji L, Pan B, Yu Y, Li W, Zhao X, He Q, Liu X, Huang Y, Liao S, Zhou B, Chui D, Chen YE, Sun Z, Dong E, Wang Y, Zheng L. Neuron. 2023;111(22):3634. https://doi.org/10.1016/j.neuron.2023.08.010.
30. a) JL, Kirkland T, Tchkonia. *J Intern Med* 2020, *288*(5), 518. https://doi.org/10.1111/joim.13141; b) *EBioMedicine* 2017, *21*, 21, https://doi.org/10.1016/j.ebiom.2017.04.013.
31. Vandenbark AA, Offner H, Matejuk S, Matejuk A. J Neuroinflammation. 2021;18(1):298. https://doi.org/10.1186/s12974-021-02355-0.
32. Chaib S, Tchkonia T, Kirkland JL. Nat Med. 2022;28(8):1556. https://doi.org/10.1038/s41591-022-01923-y.

Figures

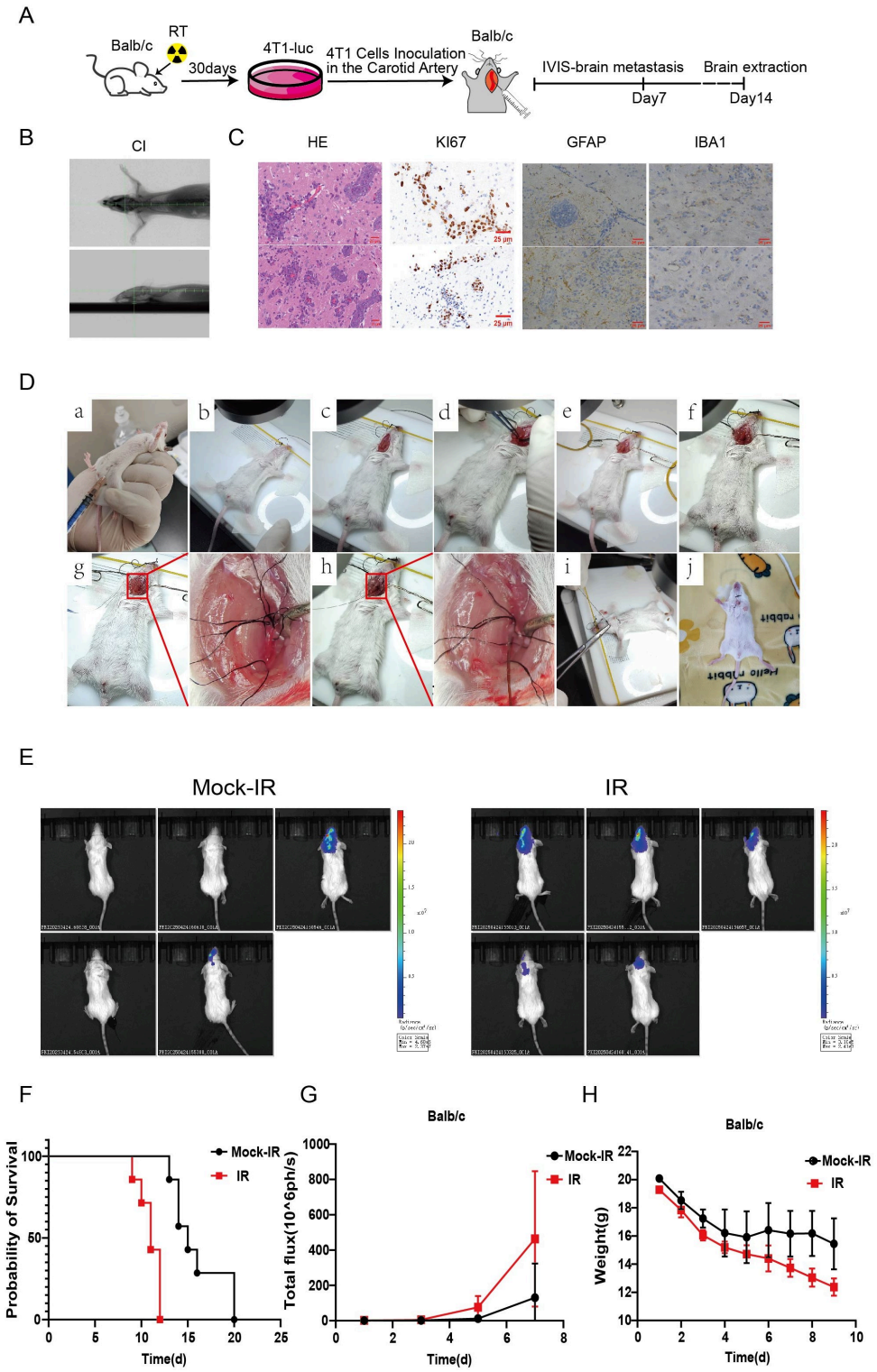


Figure 1

Murine Model of Breast Cancer Brain Metastasis after Normal Brain Irradiation

A. Experimental timeline of the animal study.

B. Schematic diagram of brain irradiation in mice at a dose of 10 Gy.

C. Representative histological images of brain tissue sections from the brain metastasis model.

D. Schematic illustration of the surgical procedure for brain metastasis model establishment via internal carotid artery injection.

E. Representative bioluminescence images showing brain metastasis progression in 4T1-luc-bearing mice from different treatment groups (control vs. irradiated, n=5 per group).

F. Kaplan–Meier survival curves comparing overall survival between control and irradiated mice after 4T1-luc cell inoculation (n=6 per cohort，P=0.0003).

G. Quantitative analysis of bioluminescence signals from brain metastases in control and irradiated mice following 4T1-luc cell injection (n=5 per group，P=0.0067).

H. Body weight changes monitored in control and irradiated mice after 4T1-luc cell inoculation (n=5 per group，P=0.004).

All experiments were independently repeated three times. Data are presented as mean ± standard deviation (SD). *P < 0.05, **P < 0.01, ***P < 0.001.

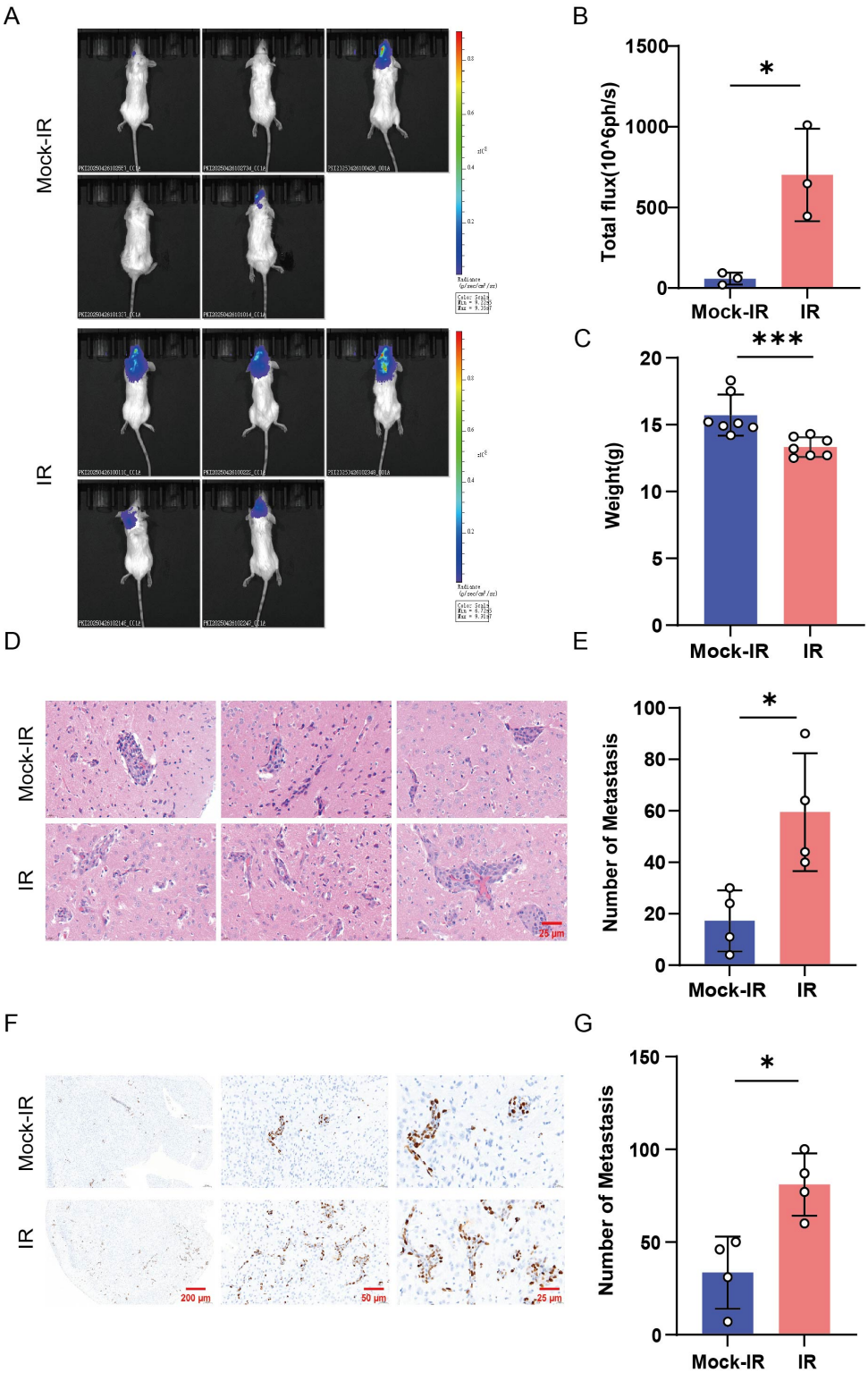


Figure 2

Normal Brain Irradiation Promotes Early Brain Colonization and Progression of Breast Cancer Metastases

A-C. Representative bioluminescence images of brain metastases (A), quantitative analysis of signal intensity (B) (n = 3 per group, P = 0.0313), and body weight changes (C) (n=8，P=0.0031) in control versus

irradiated mice on day 7 post-carotid artery injection.

D-E. Representative H&E-stained brain tissue images (D) and quantitative analysis of metastatic foci number (E) (n=4 per group，P=0.0169). Scale bar: 25 um.

F-G. Representative staining images (F) and quantification of metastatic lesions (G) (n=4 per group， P=0.0102). Scale bars: 200 um (left), 50 um (middle), and 25 um (right).

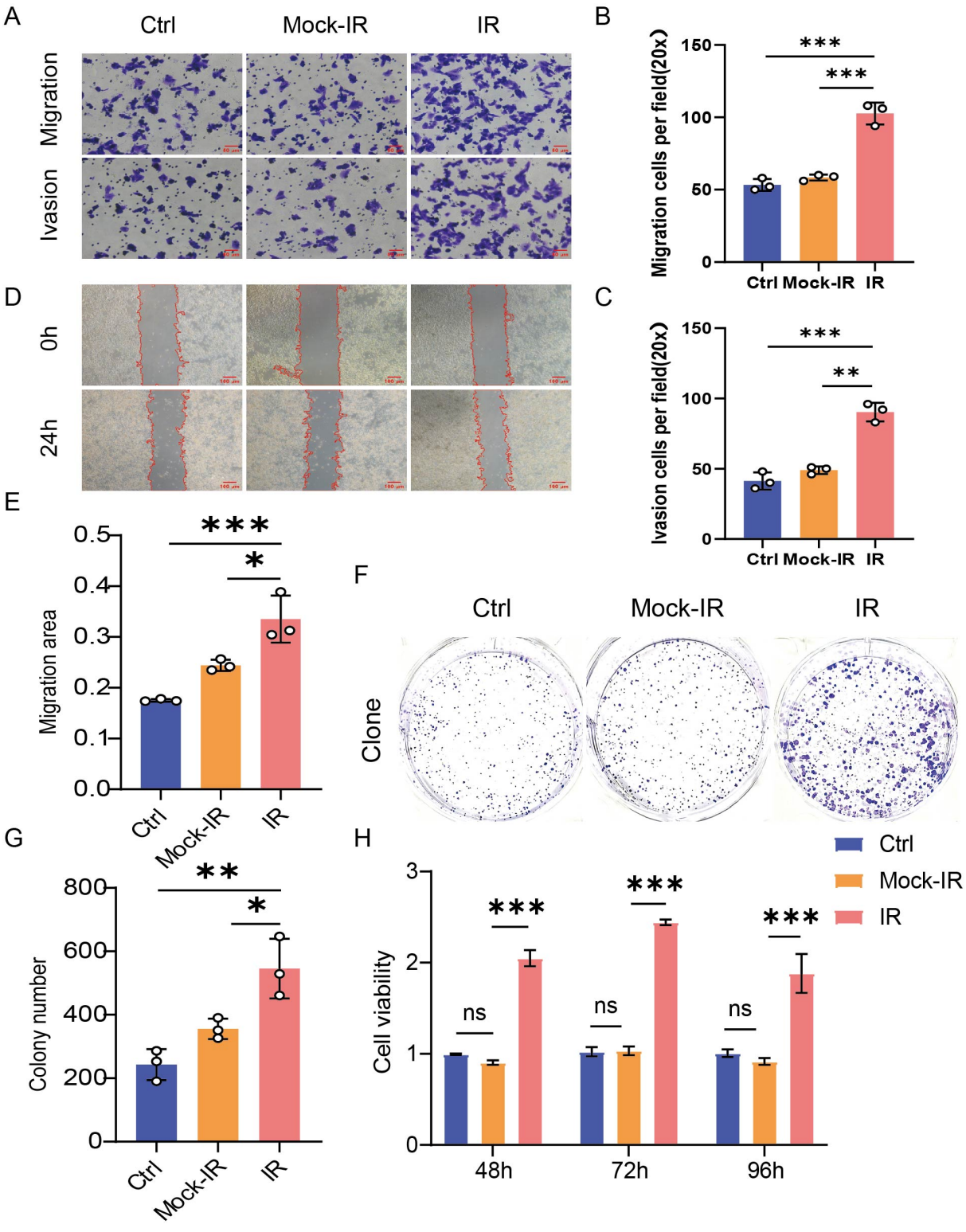


Figure 3

Normal Brain Irradiation Increased BBB Leakage and Downregulation of Tight Junction Proteins

A-B. Representative fluorescence images and quantitative analysis of FITC-dextran leakage in brain tissues from different treatment groups. Scale bar: 50 um.

C-D. Representative immunofluorescence staining images and quantitative analysis of CD31 in mouse brain tissues (n=3 per group□P=0.0011). Scale bar: 10 um.

E-F. Representative double immunofluorescence staining images and quantitative analysis of Fibrinogen and CD31 in mouse brain tissues (n=4 per group□P=0.0033). Scale bar: 10 um.

G-H. Western blotting detection and quantitative analysis of BBB-related tight junction protein expression levels in brain tissues from different treatment groups (n=3 per group□ZO-1, P=0.0064; VE-Cad, P=0.0291; Occludin, P=0.0083; Claudin5, P=0.0056).

I-J. Representative immunofluorescence staining images and quantitative analysis of ZO-1 in mouse brain tissues (n=3 per group□P=0.011). Scale bar: 50 um.

All experiments were independently repeated three times. Data are presented as mean ± standard deviation (SD). *P < 0.05, **P < 0.01, ***P < 0.001.

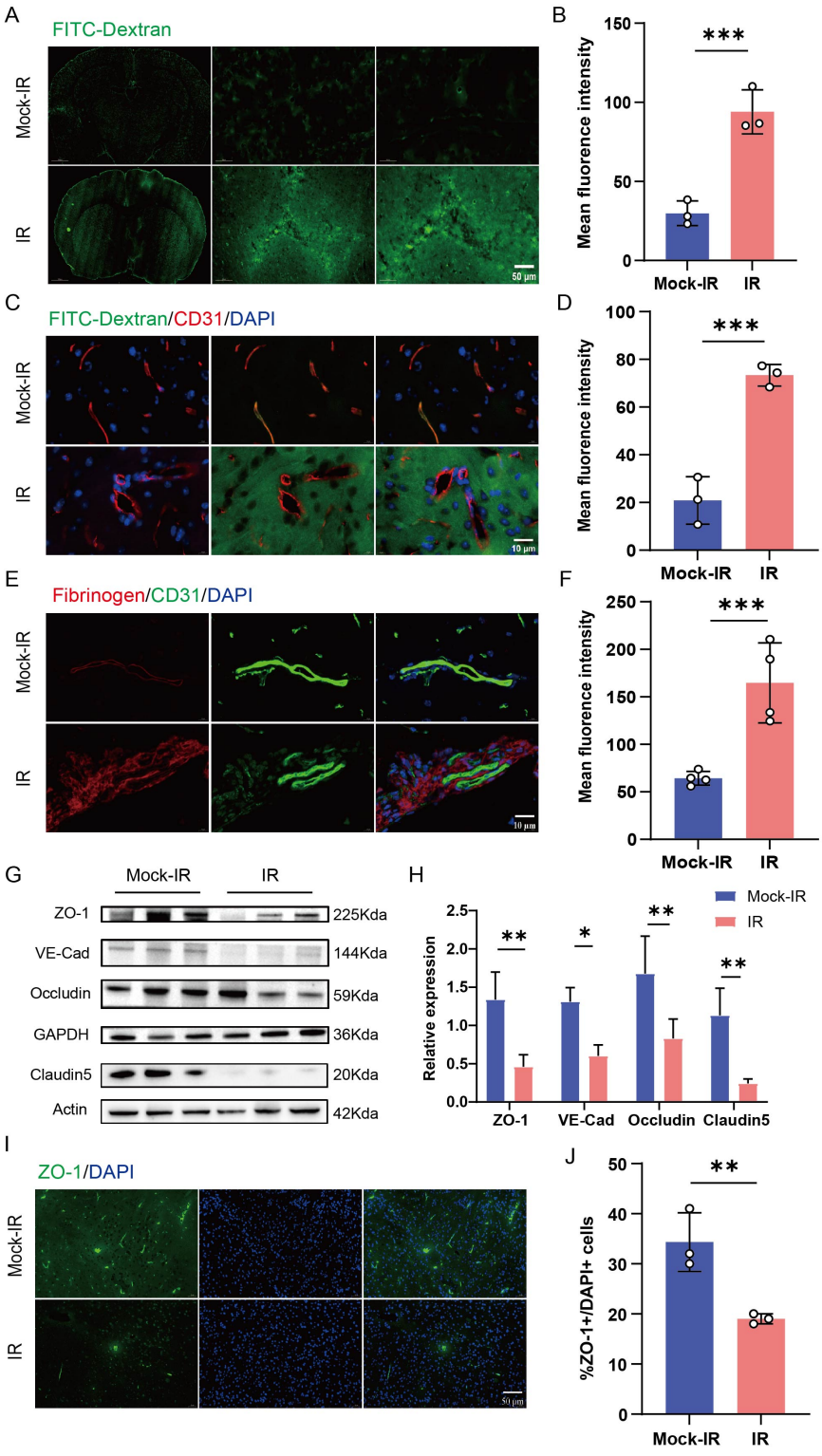


Figure 4

Irradiated Astrocytes Promote Breast Cancer Cell Migration, Invasion, and Proliferation

A-C. Transwell migration and invasion assays assessing the effects of irradiated astrocytes on the migratory and invasive capacities of 4T1 cells. Representative images (A) and quantitative analyses (B,

C), n=3 per group. Migration: $P \leq 0.001$; Invasion: Ctrl vs. IR $P < 0.001$, Mock-IR vs. IR $P = 0.002$. Scale bar: 25 um.

D-E. Wound healing assay evaluating the migration ability of 4T1 cells after co-culture. Representative images (D) and quantitative analysis (E), n=3 per group. Ctrl vs. IR $P = 0.001$, Mock-IR vs. IR $P = 0.0159$. Scale bar: 100 um.

F-G. Colony formation assay detecting the proliferative capacity of 4T1 cells. Representative images (F) and quantitative analysis (G), n=3 per group. Ctrl vs. Mock-IR $P = 0.1581$; Ctrl vs. IR $P = 0.0028$; Mock-IR vs. IR $P = 0.0253$.

H. CCK-8 proliferation assay measuring the viability of 4T1 cells at different co-culture time points, with quantitative analyses for each time point, n=3 per group, Mock-IR vs. IR $P < 0.001$.

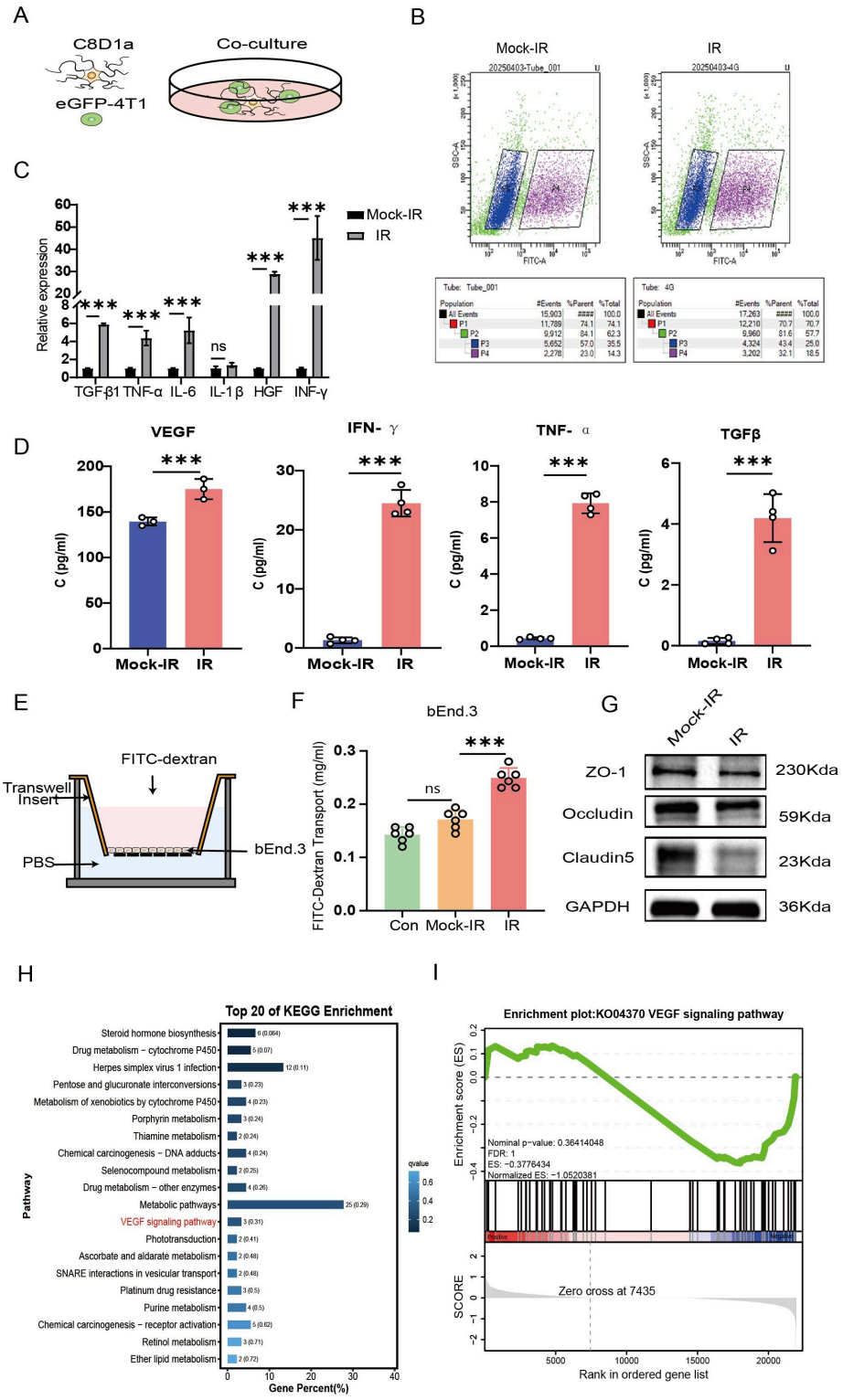


Figure 5

Secreted Factors from Irradiated Astrocyte-Breast Cancer Cell Co-Cultures Disrupt Endothelial Barrier Integrity

A. Schematic diagram of the direct contact co-culture model between C8D1A and GFP-4T1 cells.

B. Flow cytometry gating strategy following direct co-culture, showing cell population distribution. The P3 gate represents 4T1 cells, and the P4 gate represents C8D1A cells.

C. RT-PCR analysis of mRNA expression levels of secretory factors in astrocytes before and after irradiation (n=3 per group, P□0.001).

D. ELISA detection of protein expression levels of secretory factors in the supernatant of the co-culture system (n□3 per group□P□0.001).

E. Schematic illustration of the *in vitro* blood–brain barrier permeability assay using bEnd.3 cells.

F. Quantitative analysis of FITC-dextran permeability assay showing changes in bEnd.3 monolayer barrier permeability across different treatment groups (n=6 per group□P□0.001).

G. Western blotting detection of changes in tight junction protein expression levels in bEnd.3 cells.

H. KEGG pathway enrichment analysis based on transcriptome sequencing of bEnd.3 cells from different treatment groups.

I. Downregulation of the VEGF pathway in bEnd.3 cells following co-culture with irradiated astrocytes.

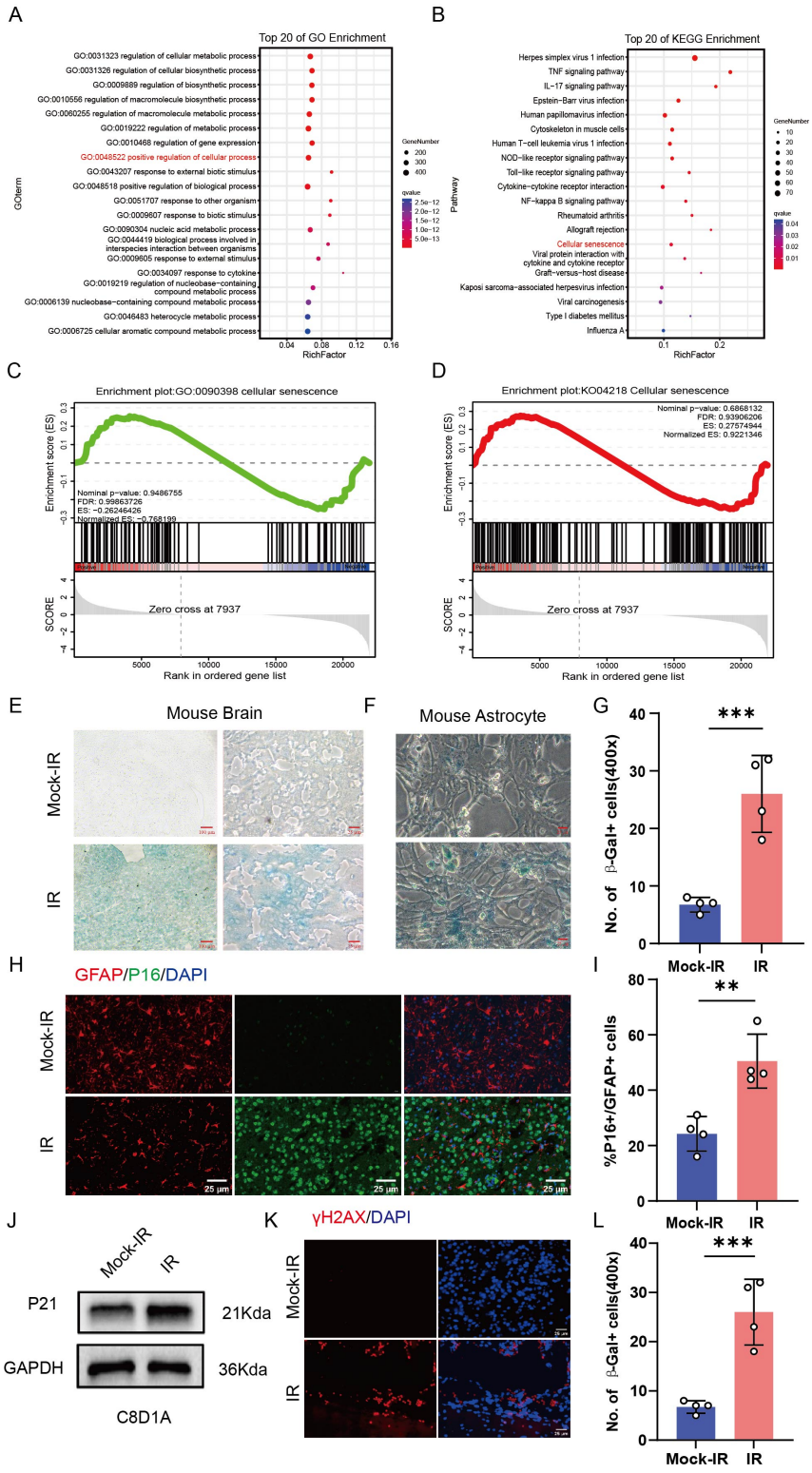


Figure 6

Normal Brain Irradiation Induces Astrocyte Senescence In Vivo and In Vitro

A-B. Transcriptome sequencing analysis of astrocytes in the control versus irradiated groups: Top 20 upregulated GO biological processes (A) and KEGG pathway enrichment analysis (B) (n=3 per group).

C-D. Cellular senescence-related pathways were significantly upregulated in both GO (C) and KEGG (D) enrichment analyses.

E. Representative images of SA-β-Gal senescence staining in mouse brain tissue (n=3 per group). Scale bars: 100 um (left) and 25 um (right).

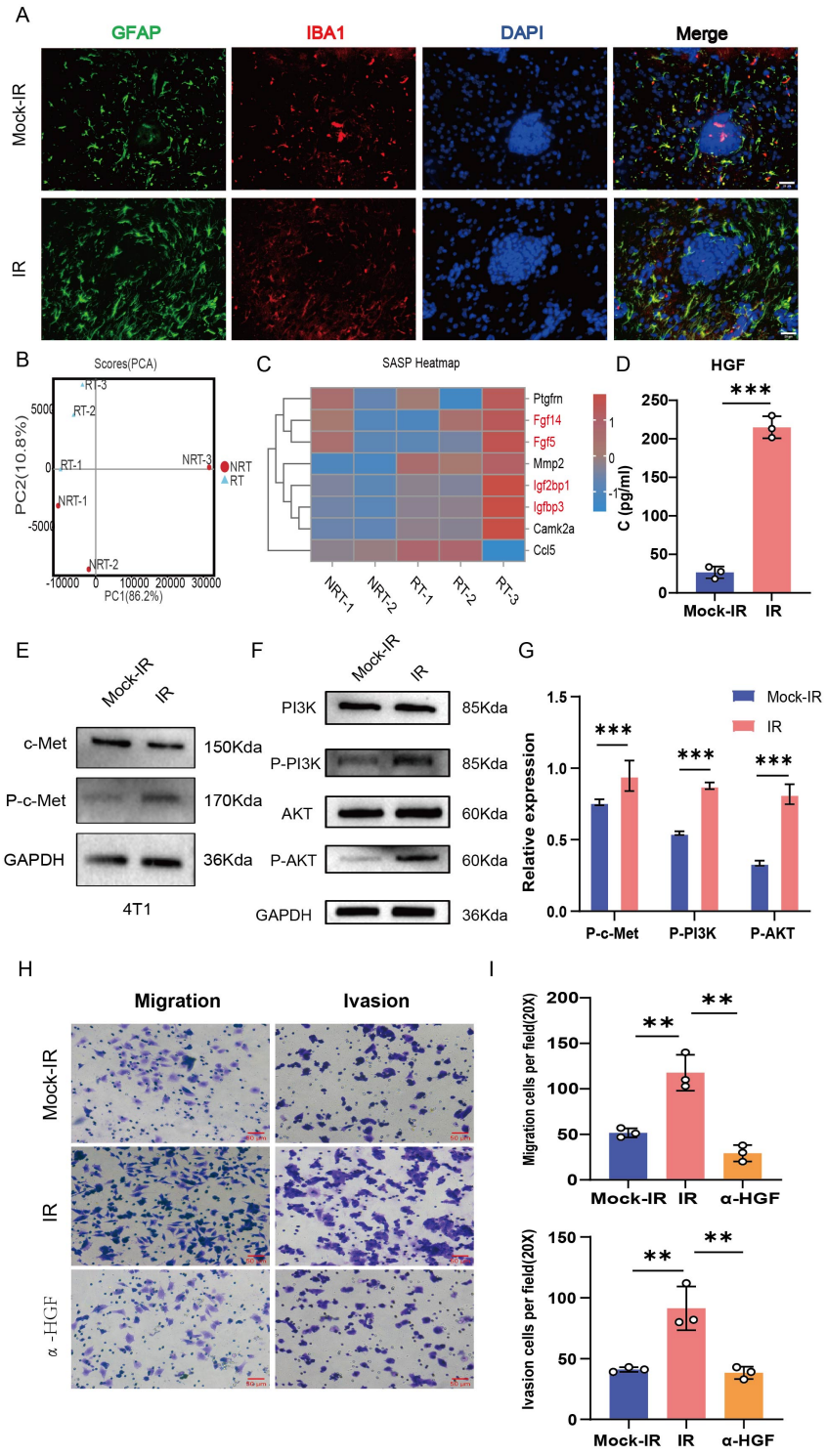
F-G. Representative images of SA-β-Gal senescence staining in mouse astrocytes (F) and quantitative analysis of the percentage of positive cells (G) (n=3 per group□P=0.0013). Scale bar: 25 um.

H-I. Representative double immunofluorescence staining images of GFAP and p16 in mouse brain tissue (H) and quantitative analysis (I) (n=4 per group□P=0.0039). Scale bar: 25 um.

J. Western blotting detection of senescence-associated protein levels (p21) in brain tissues from different treatment groups.

K-L. Representative immunofluorescence staining images and quantitative analysis of γH2AX in mouse brain tissue, reflecting DNA damage levels (n=5 per group□P□0.001). Scale bar: 25 um.

All experiments were independently repeated three times. Data are presented as mean ± standard deviation (SD). *P < 0.05, **P < 0.01, ***P < 0.001.



IF:切片-HGF/GFAP/DAPI共定位

Figure 7

Senescent Astrocyte-Derived HGF Activates c-Met/PI3K/AKT Signaling and Promotes Breast Cancer Cell Migration and Invasion

A. Representative immunofluorescence co-localization images of tumor cells with GFAP and IBA1 in brain tissue sections from mice with brain metastases. Scale bar: 25 um (n=3 per group).

B-C. Principal component analysis (PCA) of transcriptome sequencing data from mouse astrocytes (B) and analysis of differentially expressed genes related to the senescence-associated secretory phenotype (SASP) (C).

D. ELISA detection of changes in HGF protein secretion levels in the supernatant of the co-culture system (n=3 per group□P□0.001).

E-G. Western blotting detection of changes and quantitative analysis in the expression levels of c-Met, PI3K, AKT, and their phosphorylated proteins in breast cancer cells from different treatment groups (n=3 per group, P-c-Met: P=0.0038; P-PI3K: P□0.001; P-AKT: P□0.001).

H-I. Representative images and quantitative analysis of Transwell migration and invasion assays of 4T1 cells after co-culture with anti-HGF neutralizing antibody *in vitro* (n=3 per group, Migration: Mock-IR vs. IR P = 0.0018, IR vs. anti-HGF P = 0.004; Invasion: Mock-IR vs. IR P = 0.003, IR vs. anti-HGF P = 0.0023).

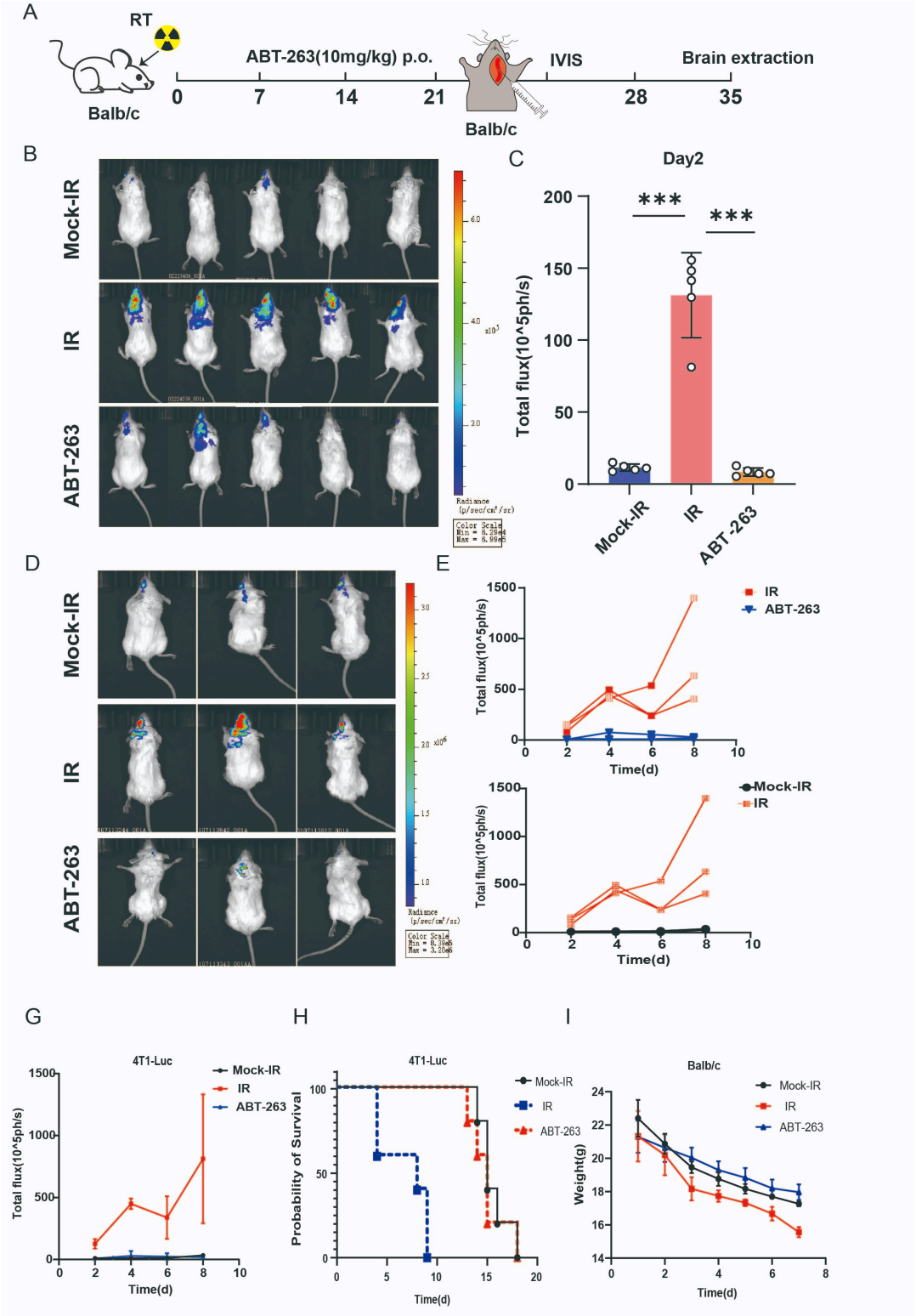


Figure 8

Clearance of Senescent Astrocytes Attenuates the Pro-Metastatic Effects of Normal Brain Irradiation and Inhibits BCBM Progression

A. Experimental flowchart of the *in vivo* rescue study.

B-C. Representative bioluminescence images (B) and quantitative analysis of photon flux (C) monitoring brain metastasis progression on day 2 after internal carotid artery inoculation of 4T1-luc cells in different treatment groups (n=5 per group□0GY vs. 10GY P□0.0001□10GY vs. ABT-263 P□0.0001).

D. Representative bioluminescence images monitoring brain metastasis progression on day 7 after internal carotid artery inoculation of 4T1-luc cells in different treatment groups.

E-G. Quantitative analysis of bioluminescence signals from brain metastases after inoculation of 4T1-luc cells in different groups (n=5 per group□0GY vs. 10GY P□0.0001□10GY vs. ABT-263 P□0.0001).

H. Kaplan–Meier survival curves comparing overall survival among different treatment groups after 4T1-luc cell inoculation (n=5 per cohort□0GY vs. 10GY P=0.0025□10GY vs. ABT-263 P=0.0025).

I. Body weight changes monitored in different treatment groups after 4T1-luc cell inoculation (n=5 per group□0GY vs. 10GY P=0.0113□10GY vs. ABT-263 P=0.003).

All experiments were independently repeated three times. Data are presented as mean ± standard deviation (SD). *P < 0.05, **P < 0.01, ***P < 0.001.

Supplementary Files

This is a list of supplementary files associated with this preprint. Click to download.

- SupplementaryMaterials.docx
- Figwb.pdf
- Figwb2.pdf